

# Hydrogenation of acetaldehyde on interstellar ice analogs reveals limited destruction

G. Molpeceres<sup>1</sup>, T. Nguyen<sup>2</sup>, Y. Oba<sup>2</sup>, and N. Watanabe<sup>2</sup>

<sup>1</sup> Departamento de Astrofísica Molecular, Instituto de Física Fundamental (IFF-CSIC), C/ Serrano 121, 28006 Madrid, Spain  
e-mail: german.molpeceres@iff.csic.es

<sup>2</sup> Institute of Low Temperature Science, Hokkaido University N19W8, Kita-ku, Sapporo, Hokkaido 060-0819 Japan  
e-mail: nguyenthanh@lowtem.hokudai.ac.jp

December 24, 2024; December 24, 2024

## ABSTRACT

**Context.** Acetaldehyde  $\text{CH}_3\text{CHO}$  is one of the most abundant interstellar complex organic molecules and its hydrogenation has important implications in several fundamental processes of interstellar chemistry, like deuterium fractionation, reactive desorption or the relation between organic functional groups of detected molecules.

**Aims.** We sought to determine which are the main hydrogenation paths of  $\text{CH}_3\text{CHO}$ . As a partially unsaturated molecule,  $\text{CH}_3\text{CHO}$  can have links with more hydrogenated species, like ethanol ( $\text{C}_2\text{H}_5\text{OH}$ ) or with more unsaturated ones, like ketene ( $\text{H}_2\text{CCO}$ ).

**Methods.** We used highly accurate quantum chemical calculations to determine the reaction rate constants for the  $\text{CH}_3\text{CHO} + \text{H/D}$  reaction. We later study, using more approximated methods, the fate of the majoritarian product of the reaction, the acetyl radical  $\text{CH}_3\text{CO}$  after subsequent reaction with hydrogen or deuterium atoms. Our theoretical results are confronted against our experiments on the hydrogenation and deuteration of  $\text{CH}_3\text{CHO}$  ice.

**Results.** We find that acetaldehyde resists hydrogenation, with only a 10% of conversion to products different than  $\text{CH}_3\text{CHO}$ . This is due to a predominance of H-abstraction at the HCO moiety, with reaction rate constants up to four orders of magnitude higher than the next possible reaction channel, that is hydrogenation at the aldehydic carbon. The formed  $\text{CH}_3\text{CO}$  radical experiences barrierless or nearly barrierless reactions in all possible reaction positions, reforming  $\text{CH}_3\text{CHO}$  and creating a closed loop that protects the molecule against hydrogenation. We constrain the branching ratios for the second reaction from experiments. Our experiments agree with the calculations and from the combination of both we can explain the presence of  $\text{H}_2\text{CCO}$ ,  $\text{CO}$ ,  $\text{CH}_4$ ,  $\text{C}_2\text{H}_5\text{OH}$ ,  $\text{H}_2\text{CO}$  or  $\text{CH}_3\text{OH}$  as minor products at the end of the reaction. We provide recommendations for future modeling efforts.

**Conclusions.** Our results show limited destruction of acetaldehyde, reinforcing the vision of this molecule as an abundant and resilient COM. From the experiments, we are not able to observe the reactive desorption of this molecule. Our results align with other modeling works, showing that the link between  $\text{CH}_3\text{CHO}$  and  $\text{C}_2\text{H}_5\text{OH}$  is not direct. Finally, our results can explain the excess of  $\text{CH}_3\text{CDO}$  found in prestellar cores.

**Key words.** ISM: molecules – Molecular Data – Astrochemistry – methods: experimental – methods: numerical

## 1. Introduction

The emergence of chemical complexity in the interstellar medium (ISM) is one of the most fascinating topics in astrochemistry. Although the concept of “complexity” is generally ill-defined, a molecule composed of six or more atoms, with at least one being carbon, is typically considered an interstellar complex organic molecule (Herbst & Van Dishoeck 2009). Given the harsh conditions in the ISM, the formation mechanisms of these molecules are vastly different from those on Earth. In the ISM, particularly within the ice-covered dust grains that account for approximately 1% of its mass (Bohlin et al. 1978), many molecules are formed through radical chemistry.

Significant effort has been devoted to studying the synthesis of complex organic molecules (COMs) on interstellar ices (Watanabe & Kouchi 2002; Fuchs et al. 2009; Rimola et al. 2014; Garrod 2013; Simons et al. 2020; Jin & Garrod 2020; Garrod et al. 2022; Enrique-Romero et al. 2022; Ferrero et al. 2023; Molpeceres et al. 2024a, to give a few representative examples). Although the processing reactions of COMs, those that convert or destroy already-formed COMs, have also garnered attention, they remain comparatively underexplored. Examples in the

literature include the systematic study of COM hydrogenation (Alvarez-Barcia et al. 2018), the hydrogenation of heterocycles (Miksch et al. 2021), and the processing of formic acid and thioformic acid (Molpeceres et al. 2022a). However, the chemical processing of COMs on interstellar grains has important implications for the evolution of chemical complexity. Among these, hydrogen abstraction (H-abstraction) reactions play a pivotal role. These reactions involve a radical (e.g., H, OH,  $\text{NH}_2$ ) abstracting a hydrogen atom from a COM, producing a closed-shell hydrogenated molecule (e.g.,  $\text{H}_2$ ,  $\text{H}_2\text{O}$ ,  $\text{NH}_3$ ) and leaving behind a parent radical of the COM. For instance, we recently demonstrated that for hydroxylamine ( $\text{NH}_2\text{OH}$ ), H-abstraction reactions, followed by O- or N-addition, can account for the apparent disappearance of this molecule in the ISM (Molpeceres et al. 2023). Besides, following similar arguments, deuterium enrichment of molecules and COMs (See, for example, the review of Ceccarelli et al. (2014)), is enhanced through H-abstraction reactions, following a cycle of H-abstraction and D-addition (Molpeceres et al. 2022a; Nguyen et al. 2021a; Lamberts & Kästner 2017b). Furthermore, the same cycle can fuel the process of reactive desorption to return the ice-synthesized molecules to the gas phase. This is due to the increase of reactive events for a fixed probabil-

ity of chemical desorption per reaction (Garrod et al. 2007), as it was evinced by chemical desorption experiments by some of us (Oba et al. 2018; Nguyen et al. 2020) on  $\text{H}_2\text{S}$  or  $\text{PH}_3$ . Clearly, H-abstraction reactions are critical components of modern astrochemical reaction networks and warrant more detailed investigation.

With advancements in astrochemistry, the pool of molecules requiring detailed study is growing not only in number but also in complexity. For instance, considering the examples of  $\text{H}_2\text{S}$  and  $\text{PH}_3$  mentioned above, these molecules have relatively simple reaction networks (Lamberts & Kästner 2017b; Molpeceres & Kästner 2021; Nguyen et al. 2021a). Starting from their atomic precursors (S and P), the fully hydrogenated molecule is the most stable product. Additionally, H-abstraction reactions exhibit increasing activation energies, while H-addition remains barrierless. These traits make such molecules easier to detect in experimental setups, as the reaction products are limited to one stable product and non-detectable reactive radicals. However, the complexity increases significantly when a carbon atom is introduced, as in carbon monosulfide (CS). Adding carbon leads to reaction networks with approximately 15 reactions en route to forming  $\text{CH}_3\text{SH}$  (Lamberts 2018; Nguyen et al. 2023), including irreversible pathways such as  $\text{CH}_3 + \text{H}_2\text{S}$ . This highlights the intricate nature of hydrogenation sequences. Studying these networks for complex organic molecules (COMs) routinely identified in cold environments (Bacmann et al. 2012; Bacmann & Faure 2014; Jiménez-Serra et al. 2021; Jiménez-Serra et al. 2016; Megías et al. 2022; Scibelli et al. 2021) becomes increasingly challenging, whether approached experimentally or theoretically.

The molecule examined in this paper, acetaldehyde ( $\text{CH}_3\text{CHO}$ ), is one of the most abundant and extensively studied complex organic molecules (COMs) that can form on ice grains (Jin & Garrod 2020; Lamberts et al. 2019; Ferrero et al. 2023; Molpeceres et al. 2024a), albeit with some challenges (Enrique-Romero et al. 2021; Ferrero et al. 2023). Acetaldehyde can also be synthesized in the gas phase (Vazart et al. 2020). Although  $\text{CH}_3\text{CHO}$  qualifies as a COM, its reaction with hydrogen remains experimentally tractable (Bisschop et al. 2007), yet interpreting the experimental results is far from straightforward. Hydrogenation of  $\text{CH}_3\text{CHO}$  reportedly produces a mixture of acetaldehyde ( $\text{CH}_3\text{CHO}$ ), ethanol ( $\text{C}_2\text{H}_5\text{OH}$ ), methane ( $\text{CH}_4$ ), carbon monoxide (CO), formaldehyde ( $\text{H}_2\text{CO}$ ), and methanol ( $\text{CH}_3\text{OH}$ ). However, the latter three products are linked through a sequential hydrogenation pathway (Watanabe & Kouchi 2002). Meanwhile,  $\text{CH}_4$  and  $\text{C}_2\text{H}_5\text{OH}$  could, in principle, arise from alternative pathways rather than the direct hydrogenation of  $\text{CH}_3\text{CHO}$ . This complexity underscores the need to better understand the precise mechanism of  $\text{CH}_3\text{CHO}$  hydrogenation.<sup>1</sup> Such a detailed understanding is essential for proposing potential deuteration pathways and assessing the likelihood of reactive desorption, as discussed earlier.

A mechanistic understanding of this reaction can only be achieved through a synergistic combination of accurate theoretical calculations and experimental work. This is the approach we adopted in this study paper where we integrate quantum chemical calculations of the hydrogenation of  $\text{CH}_3\text{CHO}$ , incorporating a rigorous treatment of nuclear quantum effects, with tailored experiments on the  $\text{CH}_3\text{CHO} + \text{H}$  reaction. Furthermore, our work aims to unify the existing knowledge on this reaction and re-

lated reactions, such as  $\text{CO} + \text{H}$  and  $\text{H}_2\text{CCO} + \text{H}$  (Watanabe & Kouchi 2002; Fuchs et al. 2009; Mondal et al. 2021; Fedoseev et al. 2022; Ibrahim et al. 2022; Ferrero et al. 2023), by resolving discrepancies where they exist or providing justified support where they align. The structure of this manuscript is as follows: In Section 2, we provide a concise overview of our methodology. Section 3 is dedicated to the presentation of our findings. In Section 4, we discuss the results, placing them in the context of experimental, modeling, and broader astrochemical perspectives. Finally, we conclude with key remarks in Section 5.

## 2. Methods

### 2.1. Computational Details

Quantum chemical calculations were performed with a twofold objective. First, we use the results of a preliminary exploration to guide our experimental search. Second, when the full experimental procedure was completed, we expanded our quantum chemical calculations to explain the experiments, leading to a self-consistent explanation of  $\text{CH}_3\text{CHO}$  chemistry under ISM conditions. We can categorize our simulations into three different categories. First, calibration calculations using a small two-water model to test the influence of explicit water molecules in the hydrogenation of  $\text{CH}_3\text{CHO}$  (Appendix A). Second, derivation of the instanton rate constants (Rommel et al. 2011; Kästner 2014) for H-addition, H-abstraction, and D-addition on  $\text{CH}_3\text{CHO}$ . Instanton theory is an unification of path integral theory and transition state theory to simulate the quantum nature of the nuclei in the reactant and transition states of a reaction. An instanton represents the most probable tunneling path, that in our formulation is discretized in a number of points or beads, and optimized to a first-order saddle point, like in conventional transition state theory. In this case an optimization of the tunneling path with maximum transition probability (or minimum Euclidean action) is carried out. Third and last, investigation of additional reactions with hydrogen in the acetyl radical ( $\text{CH}_3\text{CO}$ ), the preferred product of the first reaction with H (see Section 3). Our quantum chemical calculations are designed to prioritize accuracy in the electronic structure calculations over cluster representativity. Acetaldehyde is shown to be a COM with a relatively weak binding with the water surface (Molpeceres et al. 2022b; Ferrero et al. 2022), which normally leads to a small influence of the water matrix on the reaction rate constants (see, for example Ferrero et al. 2023; Molpeceres et al. 2024b, for two recent examples). The instanton rate constants were calculated using a sequential cooling scheme starting from a temperature close to the crossover temperature defined as:

$$T_c = \frac{\hbar\Omega}{2\pi k_B} \quad (1)$$

where  $\Omega$  corresponds to the imaginary frequency of vibration at the transition state.  $T_c$  is an estimator of the temperature at which the tunneling effects in the rate constant start to dominate over the purely thermal ones (Gillan 1987). Because the determining quantity to compare with experiments is the reaction rate constant, that we obtain from accurate semiclassical instanton theory calculations, the inclusion of surface effects in our calculations is done *via* the implicit surface approach (Meisner et al. 2017), i.e. making the rotational partition function equal to one in the calculation of the reaction rate constant. Omitting the ice matrix, allows us to use a significantly better level of theory than when including an ice matrix. In particular, the level

<sup>1</sup> In this context, “hydrogenation” refers broadly to reactions involving H atoms, with distinctions between H-abstraction and H-addition noted where relevant.

of theory used in this work is the combination of the rev-DSD-PBEP86(D4)/jun-cc-pV(T+d)Z level (i.e. double hybrid functional with a large basis set) (Kozuch & Martin 2011; Santra et al. 2019; Dunning 1989; Papajak et al. 2011; Caldeweyher et al. 2019) for the molecular geometries and molecular Hessian and the (U)CCSD(T)/aug-cc-pVTZ (Bartlett & Purvis 1978; Purvis & Bartlett 1982; Dunning 1989; Knowles et al. 1993; Woon & Dunning 1994) gold standard method for correcting the electronic energies.<sup>2</sup> This level is used for the determination of stationary points in the respective potential energy surface (PES), calculation of the zero point vibrational energies (ZPVE) and the calculation of rate constants in the interaction of H with CH<sub>3</sub>CHO. To incorporate the effect of a polar environment, that is H<sub>2</sub>O, we also computed single point energies using the conductor-like polarizable continuum (CPCM) (Truong & Stefanovich 1995; Barone & Cossi 1998; Garcia-Ratés & Neese 2020) model employing a dielectric constant extrapolated for amorphous solid water of  $\epsilon=600$  as used in recent astrochemical literature (Nguyen et al. 2019). We present models with and without CPCM correction. The hydrogenation of the CH<sub>3</sub>CO is investigated with rev-DSD-PBEP86(D4)/jun-cc-pV(T+d)Z, that is, without further coupled cluster refinement, although CPCM single points at the DFT level are also reported. The last set of calculations is carried out using a broken-symmetry DFT formalism, first converging the triplet electronic state and then rotating the orbitals of the incoming reactant (H) to guarantee the correct spin state for the system. The rate constants for the reactions starting with the CH<sub>3</sub>CO as reactant are obtained from classical transition state theory including the tunneling correction from an asymmetric Eckart barrier (Eckart 1930). The energies coming from pure broken symmetry DFT calculations are subjected to a higher error than when correcting the electronic energies with a high level method. However, the lack of a reliable single reference solution in the case of biradical species such as the ones partaking in the CH<sub>3</sub>CO + H reaction prompt us to continue with this protocol. The agreement between experiments and theory found in this work shall serve as a proxy benchmark for the validity of our method in this particular case.

All our electronic structure calculations use the ORCA 5.0.4 code (Neese et al. 2020). Geometry optimizations and instanton calculations use a developer version of the DL-FIND code (Kästner et al. 2009) interfaced with CHEMSHELL (Metz et al. 2014).<sup>3</sup>

## 2.2. Experiments

All experiments were performed using an experimental apparatus named Apparatus for Surface Reaction in Astrophysics (ASURA). The details of the ASURA system were described in previous studies (Watanabe et al. 2006; Nagaoka et al. 2007; Nguyen et al. 2020, 2021b, 2023). In brief, it consists of an ultrahigh vacuum chamber with the basic pressure of 10<sup>-8</sup> Pa; an aluminum (Al) substrate attached to a He cryostat, an atomic source, a quadrupole mass spectrometer (QMS), and a Fourier transform infrared spectrometer (FTIR). The surface temperature was regulated between 5 and 300 K.

The chemical reactions of solid acetaldehyde (CH<sub>3</sub>CHO) with H (or D) atoms were studied on both an Al substrate and compact amorphous solid water (c-ASW) at low temper-

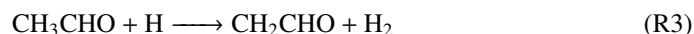
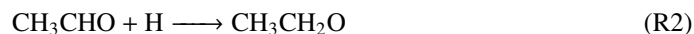
atures (typically 10 K). The c-ASW was made by the vapor deposition of water onto the substrate maintained at 110 K, with an estimated thickness of  $\sim 20$  monolayers (ML; 1 ML = 1  $\times 10^{15}$  molecules cm<sup>-2</sup>). The substrate was cooled down to 10 K after the c-ASW layer production. Gaseous CH<sub>3</sub>CHO was pre-deposited onto c-ASW with the deposition rate of 1 ML minute<sup>-1</sup>. The layer thickness of CH<sub>3</sub>CHO was adjusted to 1 ML, which was estimated using the peak area of the CO stretching band at 1728 cm<sup>-1</sup> and its absorption coefficient of 8.0  $\times 10^{-18}$  cm molecule<sup>-1</sup> (Bisschop et al. 2007). The pre-deposited CH<sub>3</sub>CHO layer was exposed to the H and D atoms produced via the dissociation of H<sub>2</sub> (or D<sub>2</sub>) in a microwave-discharged plasma in the atomic source chamber. The formed H (D) atoms were cooled to 100 K by multiple collisions with the inner wall of the Al pipe at 100 K (Nagaoka et al. 2007). The flux of H and D atoms was estimated as 5.0  $\times 10^{14}$  and 3.4  $\times 10^{14}$  cm<sup>-2</sup> s<sup>-1</sup> following the method of Oba et al. (2014), respectively. During the process of H (or D) exposure on the sample solid, interactions between CH<sub>3</sub>CHO and H (D) atoms were observed in situ using FTIR with a resolution of 2 cm<sup>-1</sup>. The reactants and products desorbed from the surface were monitored by the QMS via the temperature programmed desorption (TPD) method with a ramping rate of 4 K minute<sup>-1</sup>.

## 3. Results

### 3.1. Theoretical exploration

#### 3.1.1. Description of CH<sub>3</sub>CHO + H

The study of the H-abstraction and addition reactions necessary to rationalize our experiments begins with the evaluation of the energetics for all the possible reactions reaction channels for CH<sub>3</sub>CHO + H. The molecular structure of *syn*-CH<sub>3</sub>CHO and the atomic positions where the reaction can take place are depicted in Figure 1. For each reaction, we assume that energy dissipation occurs via the surface, treating the reactions presented in this study as elementary. The possible reactions are:



The energetic parameters for the reactions, reaction energies ( $\Delta H^R$ ), activation energies ( $\Delta H^\ddagger$ ) and imaginary frequencies of vibration at the TS ( $\Omega$ ) are gathered in Table 1. In the first place, we confirmed that all possible reactions are exothermic reactions that proceed with a moderate  $\Delta H^\ddagger$ , as is expected for closed-shell organic molecules. It is evident from the data in Table 1 that reaction R5 is, under no circumstances, competitive with reactions R1–R4, due to the extremely high activation energies. This conclusion allows us to determine that all CH<sub>4</sub> and their isotopologues are formed in the experiment from radical-radical recombinations from secondary products of the reaction (See Section 4.1). The other reactions present barriers between  $\sim 20$ –50 kJ mol<sup>-1</sup> with varying values of  $\Omega$ . For example, the reactions with the two lowest  $\Delta H^\ddagger$  also show the lowest  $\Omega$ . To be completely certain of the dominant reaction product, a kinetic analysis is required. Despite such an analysis being carried out in Section 3.1.2, a qualitative assessment of the influence of quantum tunneling can be done from the reaction coordinate (IRC) profiles.

<sup>2</sup> Details on how to run the rev-DSD-PBEP86(D4) calculations with different codes can be found at <https://www.compchem.me/revdsd-pbep86-functional>

<sup>3</sup> Cartesian coordinates supporting the calculations can be found at <https://zenodo.org/records/14278652>

**Table 1.** Reaction enthalpies ( $\Delta H^R$ , kJ mol<sup>-1</sup>), activation energies ( $\Delta H^\ddagger$ , kJ mol<sup>-1</sup>), the absolute value of the imaginary frequency of vibration ( $\Omega$ , cm<sup>-1</sup>) and crossover temperature ( $T_c$ , K) for the reactions of CH<sub>3</sub>CHO with H. We report both the results of the model including implicit interaction with the water matrix (labeled CPCM) and excluding it at the (U)CCSD(T)/aug-cc-pVTZ/revDSD-PBEP86(D4)/jun-cc-pV(T+d)z level.

Reaction	Label	$\Delta H^R / \Delta H^R_{\text{CPCM}}$	$\Delta H^\ddagger / \Delta H^\ddagger_{\text{CPCM}}$	$\Omega / T_c$
CH <sub>3</sub> CHO + H $\longrightarrow$ CH <sub>3</sub> CO + H <sub>2</sub>	R1	-63.1 / -55.7	18.5 / 23.9	1450i / 332
CH <sub>3</sub> CHO + H $\longrightarrow$ CH <sub>3</sub> CH <sub>2</sub> O	R2	-60.3 / -54.2	31.0 / 31.2	1260i / 289
CH <sub>3</sub> CHO + H $\longrightarrow$ CH <sub>2</sub> CHO + H <sub>2</sub>	R3	-32.7 / -31.5	41.2 / 40.8	1644i / 377
CH <sub>3</sub> CHO + H $\longrightarrow$ CH <sub>3</sub> CHOH	R4	-101.3 / -101.1	47.3 / 51.2	2005i / 459
CH <sub>3</sub> CHO + H $\longrightarrow$ CH <sub>4</sub> + HCO	R5	-86.6 / -76.7	142.6 / 145.4	1597i / 366

**Notes.**  $\Delta H^R$  and  $\Delta H^\ddagger$  are determined from a preconverged pre-reactant complex (PRC) as  $\Delta H^{R,\ddagger} = H_{\text{Prod,TS}} - H_{\text{PRC}}$ . ZPVE are determined at the rev-DSD-PBEP86(D4)/jun-cc-pV(T+d)Z level

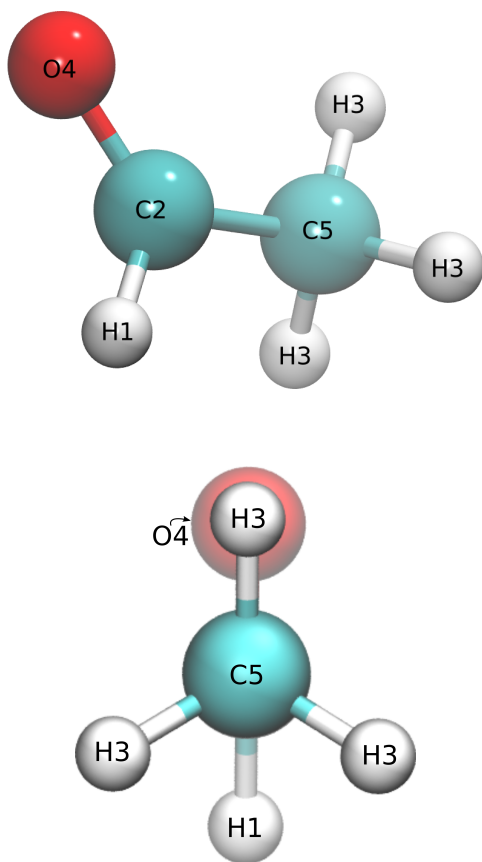


**Fig. 1.** Top. Acetaldehyde molecule with the positions where the hydrogenation and deuteration reactions are sampled. Bottom. Newman projection of the molecular model showing the considered CH<sub>3</sub>CHO *syn* conformer

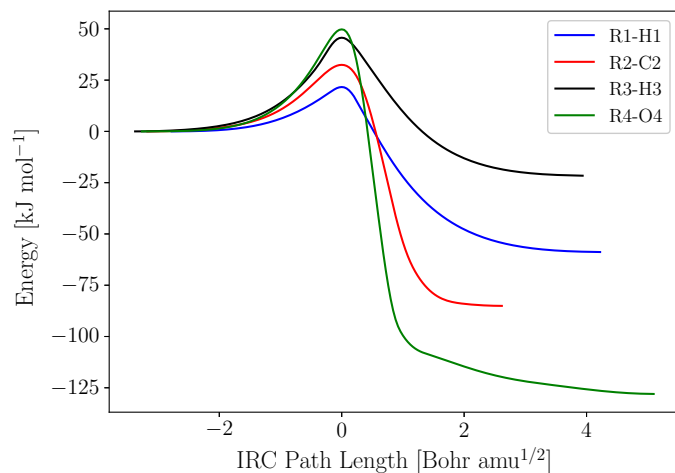


**Fig. 2.** IRC profiles for reactions R1–R4 (We omit reaction R5 due to the high  $\Delta H^\ddagger$ ). IRC profiles are presented at the rev-DSD-PBEP86(D4)/jun-cc-pV(T+d)Z not corrected by ZPVE, double-level CCSD(T), or implicit water ice environment (CPCM).

### 3.1.2. Kinetic Analysis and reactions with Deuterium

We begin our instanton calculations using the sequential cooling scheme at a temperature of approximately  $0.7T_c$ , starting from a closed instanton path consisting of 36 beads. As described in Section 2, we progressively converge the instanton paths at lower temperatures. To ensure convergence with respect to the number of beads at low temperatures, we increase the number of beads to 70 for temperatures below approximately 140 K in all reactions. The hydrogenation rate constants,  $k_H$ , are presented in Figure 3. We omit the calculation of rate constants for Reaction R5 because instanton calculations are computationally demanding, and this reaction has too high an activation energy to be competitive. The rate constants are computed down to different lower temperature limits for each reaction. This variation arises because the convergence of instanton paths depends on the reaction, with the abstraction on the CH<sub>3</sub> moiety being particularly challenging to converge. However, in the cases we studied, the rate constants are converged or close to the asymptotic tunneling limit, so  $k_H(T_{\text{last}}) \approx k_H(10)$ . Since the reaction outcome is dominated by Reaction R1, the lack of rate constants at temperatures below 50 K for Reactions R3 or R4 does not affect our conclusions. It is worth noting that the effect of the implicit solvation scheme varies among different reactions, with Reactions

Such IRC profiles can be visualized in Figure 2. From them, we observe that both reactions R1 and R3 have wider barriers than reactions R2 and R4. Besides, both H-addition reactions, R2 and R4, are also more exothermic, which has also an impact on the tunneling probability. Overall, based on the energetics and  $T_c$  (Equation 1) it is not possible to determine which is the dominant product of the reaction. Kinetic simulations such as the ones in Section 3.1.2 are necessary to discriminate them.

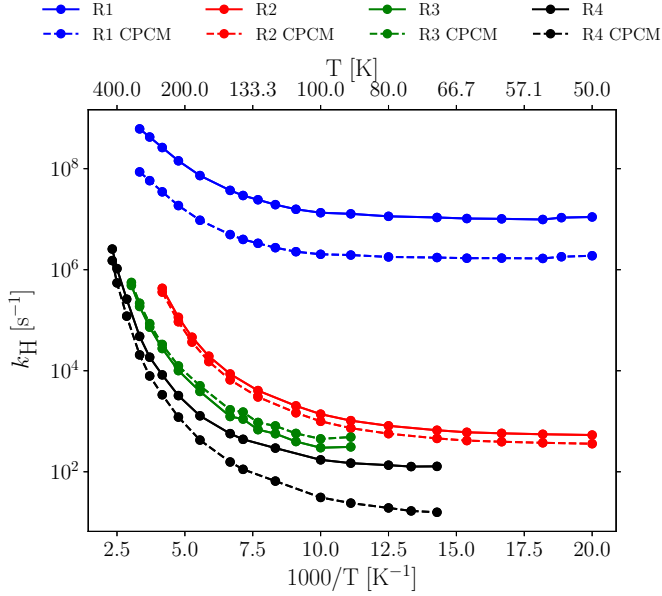
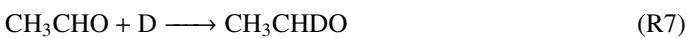


**Fig. 3.** Arrhenius plot of the hydrogenation rate constants ( $k_H$ ) for reactions R1–R4 including (dashed lines) and without including (solid lines) an implicit solvation model. All rate constants are corrected for implicit surface. Rate constants are presented until lowest temperature achievable for each instanton in the sequential cooling scheme.

R1 and R4 showing the most significant changes. Specifically, at low temperatures, these reactions are slower when considering an implicit water matrix due to the increase in  $\Delta H_{\text{CPCM}}^\ddagger$  found for the reactions. Nevertheless, this increase does not alter the overall kinetics of the system regarding competitive reaction pathways.

A quick inspection of Figure 3 reveals that Reaction R1 is the fastest across all temperatures, consistently dominating over all other reaction pathways. Furthermore, aside from Reaction R1, all other reactions exhibit rate constants that are competitive with hydrogen atom diffusion (Asgeirsson et al. 2017; Senevirathne et al. 2017), with diffusion rates ( $k_{\text{Diff}}$ ) in typical potential sites ranging from  $10^3$  to  $10^5$  s $^{-1}$  at 10 K (see, for example, Figure 7, bottom panel of Senevirathne et al. 2017). This competition suggests that even if a pre-reactive complex favoring reactions other than Reaction R1 is formed—perhaps due to a favorable orientation of the radical attack—diffusion away from the reaction site in a reaction-diffusion competition (Chang et al. 2007) will either completely or partially suppress these alternative reaction pathways. Consequently, we conclude that Reaction R1 is the sole outcome of the  $\text{CH}_3\text{CHO} + \text{H}$  reaction. This conclusion allows us to rationalize the results obtained in our experiments (see Section 3.1.3).

We also examined deuteration rate constants,  $k_D$ . For these calculations, we focused on the H1 and C2 positions. For example:



because they have the lowest  $\Delta H^\ddagger$  and the highest  $k_H$ . The rate constants are shown in Figure 4. In both cases we observe a reduction of  $k_D$  over  $k_H$  due to the reduced efficiency of quantum tunneling. The kinetic isotope effects (KIE; calculated as

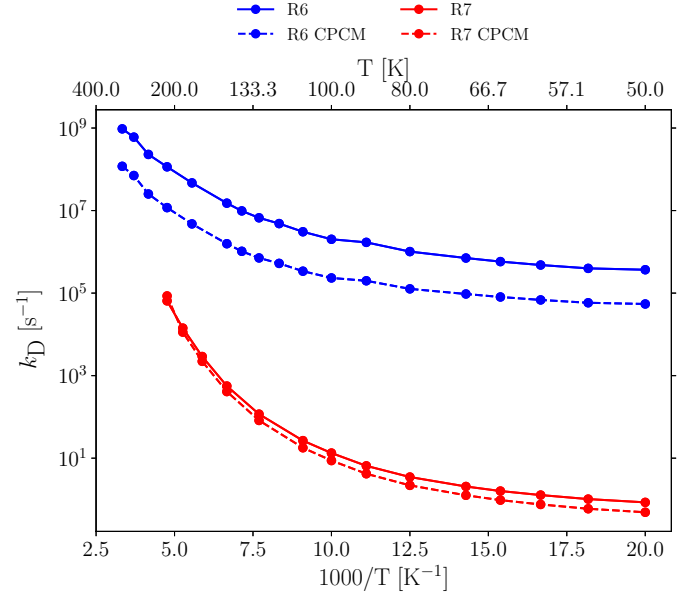
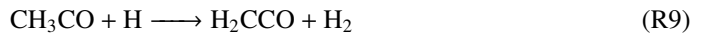


**Fig. 4.** Similar to Figure 3 but including deuterium as incoming particle ( $k_D$ ) for reactions R6 and R7

$k_H / k_D$ ) at 50 K $^4$  that we observe according to our calculations are,  $\text{KIE}_{\text{R1/R6}}=34.7$  and  $\text{KIE}_{\text{R2/R7}}=734.1$ , calculated including the implicit solvent approach. The KIE is larger in the case of reaction R7, because this reaction is a D addition and quantum tunneling is reduced, compared to reaction R6, which is an H abstraction and has a higher tunneling probability.

### 3.1.3. Hydrogenation of the $\text{CH}_3\text{CO}$ radical

The reaction  $\text{CH}_3\text{CHO} + \text{H}$  leads almost exclusively to  $\text{CH}_3\text{CO}$ . Therefore, the  $\text{CH}_3\text{CHO}$  reaction network must be completed by relying on the chemistry of such a radical. In this section we study the hydrogenation of  $\text{CH}_3\text{CO}$  following a scheme similar to that shown in Figure 1 (only this time without the H1 position). The study of the  $\text{CH}_3\text{O} + \text{H}$  reaction has the peculiarity that it should be studied in the open-shell singlet channel, i.e. using a biradical wavefunction. Radical-radical reactions generally show lower barriers than the radical-closed shell reactions, so we first check which of the following reactions are barrierless using PES scans:



The scans for the barrierless reactions are shown in Figure 5. Of all the above reactions, only reaction R11 was not found to be barrierless. All other reactions show a barrierless profile. We remark the difficulty of obtaining clean scans for these, except for reaction R8, because in the latter case there are no competing channels in the direction of the scan. The other scans

<sup>4</sup> While we formally calculate  $k_{\text{H,D}}$  down to 50 K, an extrapolation to 10 K would not change the KIE significantly as R1, R6, R2 and R7 are almost at the horizontal asymptote characteristic of unimolecular deep tunneling (Figures 3 and 4).

**Table 2.** Similar to Table 1, but for the  $\text{CH}_3\text{CO} + \text{H}$  reaction. We added a column  $k_{\text{Eckart}}^{50}$  denoting the rate constant at 50 K ( $\text{s}^{-1}$ ) computed using an asymmetric Eckart fit to the barrier in reaction R11 with/without CPCM correction. All values are reported at the revDSD-PBEP86(D4)/jun-cc-pV(T+d)z level with and without including implicit solvent corrections. The A(B) notation symbolizes  $\text{A} \times 10^B$ .

Reaction	Label	$\Delta H^{\text{R}} / \Delta H_{\text{CPCM}}^{\text{R}}$	$\Delta H^{\ddagger} / \Delta H_{\text{CPCM}}^{\ddagger}$	$\Omega$	$k_{\text{Eckart}}^{50} / k_{\text{Eckart, CPCM}}^{50}$
$\text{CH}_3\text{CO} + \text{H} \longrightarrow \text{CH}_3\text{CHO}$	R8	-398.9 / -406.1 <sup>a</sup>	N/A <sup>b</sup>	N/A <sup>b</sup>	N/A <sup>b</sup>
$\text{CH}_3\text{CO} + \text{H} \longrightarrow \text{H}_2\text{CCO} + \text{H}_2$	R9	-298.8 / -296.6 <sup>a</sup>	N/A <sup>b</sup>	N/A <sup>b</sup>	N/A <sup>b</sup>
$\text{CH}_3\text{CO} + \text{H} \longrightarrow \text{CH}_3\text{COH}$	R10	-154.9 / -179.1 <sup>a</sup>	N/A <sup>b</sup>	N/A <sup>b</sup>	N/A <sup>b</sup>
$\text{CH}_3\text{CO} + \text{H} \longrightarrow \text{CH}_4 + \text{CO}$	R11	-395.3 / -387.9	13.2 / 16.2	928i	2.0(7) / 1.4(6) <sup>c</sup>

**Notes.** <sup>a</sup> - Calculated from the bimolecular system as  $\Delta H^{\text{R}} = H_{\text{Prod}} - (H_{\text{CH}_3\text{CO}} + H_{\text{H}})$  <sup>b</sup> - Barrierless. <sup>c</sup> - Unimolecular rate constants obtained using a reactant state at large  $\text{CH}_3\text{CO}$  and H distance, as converging a pre-reactant complex was impossible due to the barrierless channels presence nearby.

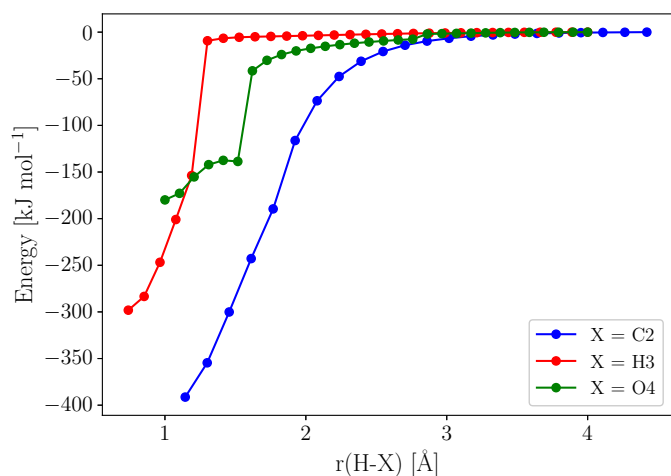


**Fig. 5.** Potential energy scan for Reactions R8 (blue curve), R9 (red curve) and R10 (green curve) at the revDSD-PBEP86(D4)/jun-cc-pV(T+d)z level using a broken symmetry formalism. The discontinuities in  $r(\text{H-H3})$  and  $r(\text{H-O4})$  are caused by insufficient resolution of the PES scan. The small bump in  $r(\text{H-O4})$  is attributed to the constraints in the C-H bonds required to carry out the scan (See text).

have discontinuities that we attribute to a combination of a low resolution and hindered conformational changes from competitive barrierless pathways during the coordinate scan. For example, the scan for reaction R10 shows a small bump at about 1.4 Å. This is due to the fact that in this scan we had to constrain the C-H ( $\text{CH}_3$  moiety) bond distance to prevent the optimizer from visiting the barrierless reaction R9 at long distances. This results in a small stiffness of the structure leading to this bump. Our calculations still predict the barrierless reaction. We recall that the calculations involving these reactions are carried out using a broken-symmetry formalism, at the revDSD-PBEP86(D4)/jun-cc-pV(T+d)z level, without correction with coupled-cluster methods. This, combined with the also approximate nature of the CPCM implicit solvent scheme, makes the second set of calculations less accurate than those shown in section 3.1.1. The energetic values for the reactions are collected in Table 2. From the table we can see that the  $\Delta H^{\ddagger}$  for reaction R11 (counterpart of R5) is significantly lower in this second set than in the previous reactions for the hydrogenation of acetaldehyde. We also observe the effect of the implicit solvation correction on some energetic parameters of the reaction. The abundant presence of  $\text{CH}_4$  and its isotopologues in our ex-

periments supports the reaction R11, even with a barrier (see next paragraph and section 3.2.1 and 4.1). Although our results for this reaction are qualitative, they are in agreement with the experiments. However, for a more detailed study of R11, we suggest using multireference methods. All other reactions are barrierless. Finally, it is also worth noting that our results in this section are not affected by deuteration, since tunneling does not determine the viability of the reaction (for reactions R8-R10) or does not contribute significantly (reaction R11, which requires the fragmentation of a C-C bond).

The possibility of finding products beyond those obtained in barrierless channels can be easily rationalized if we consider the typical reaction-diffusion competition scheme (Chang et al. 2007). Assuming that the desorption of both reactants and the diffusion of  $\text{CH}_3\text{CHO}$  are negligible, the rate constant for the reaction under this formalism is (Chang et al. 2007):

$$k = \frac{k_{\text{R}}}{k_{\text{R}} + k_{\text{Diff}}}, \quad (2)$$

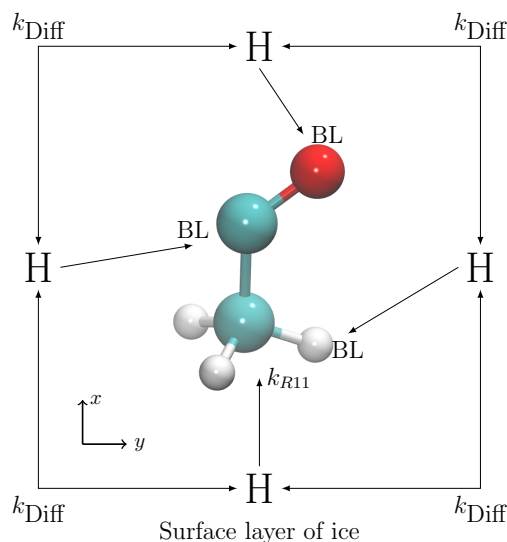


**Fig. 6.** Schematic view of the  $\text{CH}_3\text{CO} + \text{H}$  reaction. Depending on the initial configuration of the H atoms, the different  $k_{\text{R}}$  must compete with diffusion,  $k_{\text{Diff}}$ . If  $k_{\text{R}} \gg k_{\text{Diff}}$ , then the reaction would dominate even in the presence of a barrierless channel, as shown in the figure. BL means barrierless.

where “R” and “Diff” represent reaction and diffusion. In the anisotropic potential created by an amorphous polar environment such as ASW, the orientation from which H atoms approach is random. Assuming that all directions are equally possible for reactions R8–R11, the equation 2 shows that if each reaction starts from different positions, as is the case, then moving out of the reaction center requires at least one diffusion step. If  $k_R$  is much larger than  $k_{\text{Diff}}$ , then the reaction can start from that orientation, even if a barrierless channel is available. This is essentially different from gas phase reactivity. A scheme for this explanation is shown in figure 6. The arguments based on reaction-diffusion competition are therefore able to rationalize the experimental results in the light of the theoretical calculations, as we show in Section 4.1. However, not all reaction orientations are equally weighted, resulting in different branching ratios for reactions. Determining the exact branching ratios for these barrierless reactions from theoretical calculations is challenging. The same arguments presented in this section apply to the reactions studied in section 3.1.1 (reactions R1–R5), but in this case reactions other than reaction R1 are competitive with diffusion,  $k_R \sim k_{\text{Diff}}$ , and therefore reaction R1 is dominant.

Our theoretical results for the hydrogenation of  $\text{CH}_3\text{CO}$  are in reasonable agreement with those presented in Ibrahim et al. (2022), although several differences appear. In their study, Ibrahim et al. (2022) indicate that the reaction R11 is barrierless, while the reaction R9 has an activation energy of  $\sim 18 \text{ kJ mol}^{-1}$ . This tendency contradicts our calculations and experiments. However, this discrepancy does not change the picture of both works, except for the absence of  $\text{H}_2\text{CCO}$  by reaction R9, which we found very fast, and which is supported by experiments, since all other reactions remain very fast in both our works. We believe that the reason for the discrepancy could be a non-biradical wavefunction in the case of Ibrahim et al. (2022). Starting our calculations from an ionic wavefunction, we can reproduce the results of Ibrahim et al. (2022) for the reaction R9 with even higher activation energies ( $\sim 30 \text{ kJ mol}^{-1}$ ).

## 3.2. Experiments

### 3.2.1. Hydrogenation experiments

Figure 7 shows an FTIR spectrum of the solid  $\text{CH}_3\text{CHO}$  on c-ASW at 10 K. The most intense absorption peak at  $1728 \text{ cm}^{-1}$  was attributed to the C-O stretching band ( $\nu_s \text{C}=\text{O}$ ) in  $\text{CH}_3\text{CHO}$ . Additionally, other infrared bands were observed at 1432, 1349, and  $1124 \text{ cm}^{-1}$  can be assigned to the  $\text{CH}_2$  scissors,  $\text{CH}_3$  symmetric deformation, and C-C stretch of the solid  $\text{CH}_3\text{CHO}$ , respectively (Bennett et al. 2005; Bisschop et al. 2007).

Figure 8(a) shows the difference spectrum of solid  $\text{CH}_3\text{CHO}$  after exposure to H atoms for up to 2 hours compared to the initial spectrum of unexposed  $\text{CH}_3\text{CHO}$ . The intensity of the C-O stretching band at  $1728 \text{ cm}^{-1}$  decreased with atom exposure time, indicating the loss of  $\text{CH}_3\text{CHO}$ . Figure 8(b) shows variations in the relative abundance of  $\text{CH}_3\text{CHO}$  after exposure to H atoms at 10 K with relevance to atom exposure times, with a blank experiment for  $\text{H}_2$  exposure. The consumption of  $\text{CH}_3\text{CHO}$  was estimated to be only 10% relative to the initial amount of  $\text{CH}_3\text{CHO}$  after exposure to H atoms for up to 2 hours, while no decrease was observed after exposure to  $\text{H}_2$  molecules. We expect the formed  $\text{CH}_3\text{CO}$  radicals from reaction R1 to further react with H atoms on the surface according to the reactions (R8 - R11). Unfortunately, we could not observe any distinct infrared features for products from the pre-deposition of  $\text{CH}_3\text{CHO}$  and H atoms on c-ASW at 10 K, probably because of the small

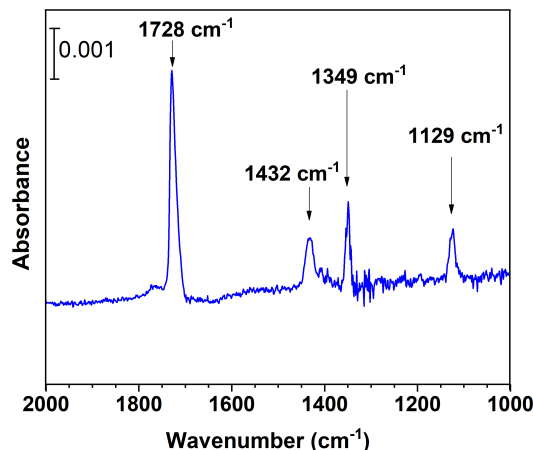


Fig. 7. Fourier-transform infrared profile of  $\text{CH}_3\text{CHO}$  on c-ASW at 10 K

amount of products. The loss of  $\text{CH}_3\text{CHO}$  may be partially due to reactive desorption. We cannot quantitatively evaluate this in any of our experiments, even considering the low desorption energy of  $\text{CH}_3\text{CHO}$  of  $\sim 3500 \text{ K}$  (Molpeceres et al. 2022b; Ferrero et al. 2022), something we discuss in more detail in section 4.2.

The TPD experiments demonstrated the formation of  $\text{CH}_4$  and CO based on the desorption peak observed at  $m/z = 16$  and  $m/z = 28$  in the temperature range of 30–60 K and 25–35 K, respectively (Figure 9, top and middle panels). These results are in agreement with the computational predictions for the reaction (R11) (see Section 3.1.3) and (Ibrahim et al. 2022) experiments. In addition, we observed a desorption peak at  $m/z = 46$  in the desorption temperature range 150 - 165 K (Figure 9, bottom panel), suggesting the formation of ethanol ( $\text{C}_2\text{H}_5\text{OH}$ ). This ethanol should be formed by the H addition reaction of  $\text{CH}_3\text{COH}$ , which was obtained from the reaction R10, followed by:



No distinct IR features of the products of the reaction between  $\text{CH}_3\text{CHO}$  and H atoms were observed in the pre-deposition experiments, probably due to the small amount of solid  $\text{CH}_3\text{CHO}$  (1 ML). In order to identify the products of the reaction between  $\text{CH}_3\text{CHO}$  and H atoms in more detail by FTIR, we performed an additional experiment in which 30 ML of  $\text{CH}_3\text{CHO}$  was co-deposited with H atoms on the Al substrate at 10 K, a technique suitable for identifying reaction products. Figure 10 shows an FTIR spectrum obtained after co-deposition of  $\text{CH}_3\text{CHO}$  with H atoms on Al substrate at 10 K. In contrast to the behavior of the pre-deposited  $\text{CH}_3\text{CHO}$  with H atoms (Figure 8a), various peaks appeared after the co-deposition of  $\text{CH}_3\text{CHO}$  with H atoms. The appearance of a sharp peak at  $2133 \text{ cm}^{-1}$  was assigned to CO (Gerakines et al. 1995). After its formation on the surface, CO should be further hydrogenated to give formaldehyde ( $\text{H}_2\text{CO}$ ) and methanol ( $\text{CH}_3\text{OH}$ ), with peaks at  $1724$  and  $1500 \text{ cm}^{-1}$  for  $\text{H}_2\text{CO}$  (Hidaka et al. 2004) and  $1044 \text{ cm}^{-1}$  for  $\text{CH}_3\text{OH}$  (Nagaoka et al. 2007) as observed in the spectrum (Figure 10). A strong peak observed at  $1305 \text{ cm}^{-1}$  was attributed to  $\text{CH}_4$ , which was in good agreement with the C-H stretching band of  $\text{CH}_4$  (Qasim et al. 2020). In addition, two

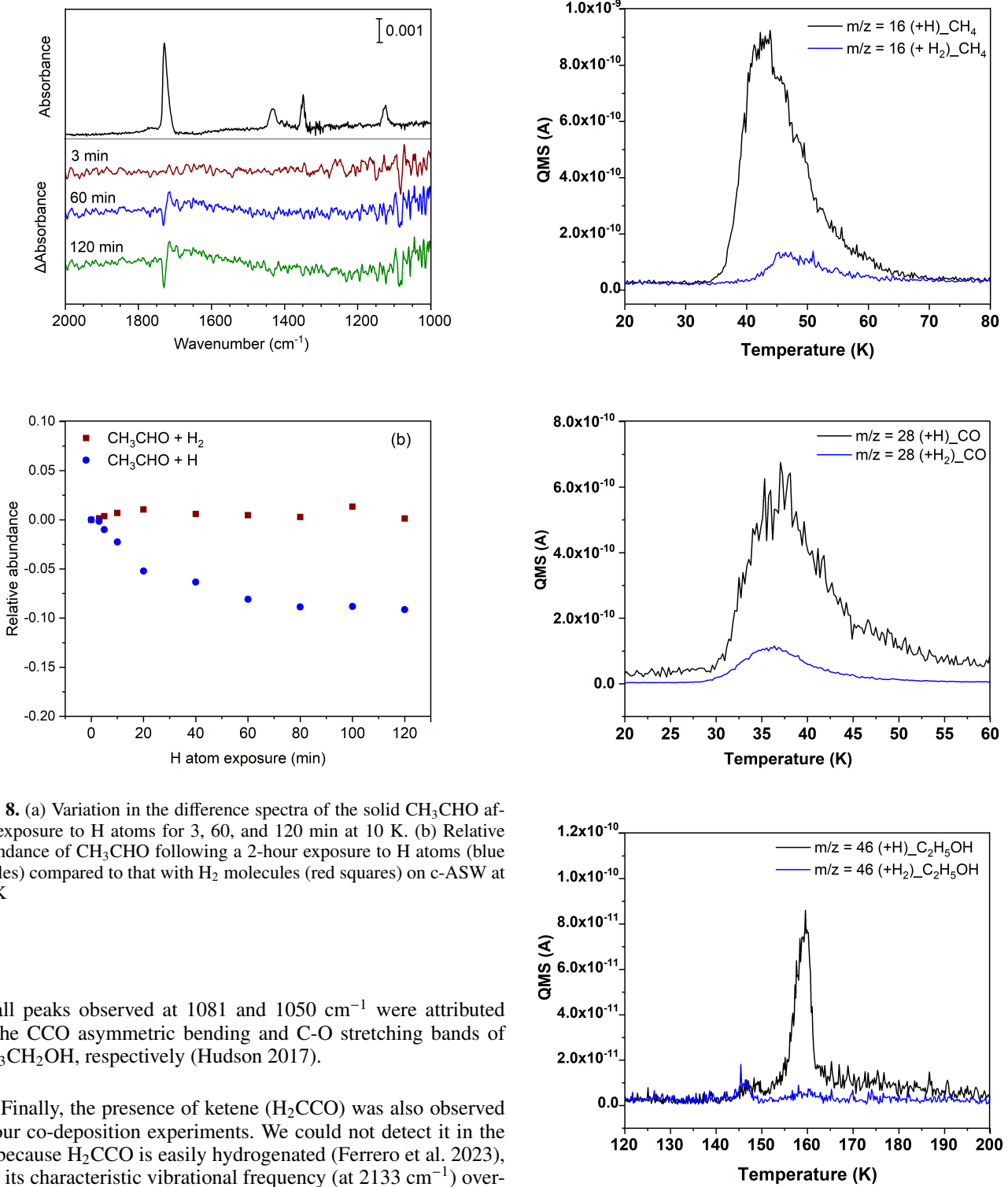


**Fig. 8.** (a) Variation in the difference spectra of the solid  $\text{CH}_3\text{CHO}$  after exposure to H atoms for 3, 60, and 120 min at 10 K. (b) Relative abundance of  $\text{CH}_3\text{CHO}$  following a 2-hour exposure to H atoms (blue circles) compared to that with  $\text{H}_2$  molecules (red squares) on c-ASW at 10 K

small peaks observed at  $1081$  and  $1050 \text{ cm}^{-1}$  were attributed to the CCO asymmetric bending and C-O stretching bands of  $\text{CH}_3\text{CH}_2\text{OH}$ , respectively (Hudson 2017).

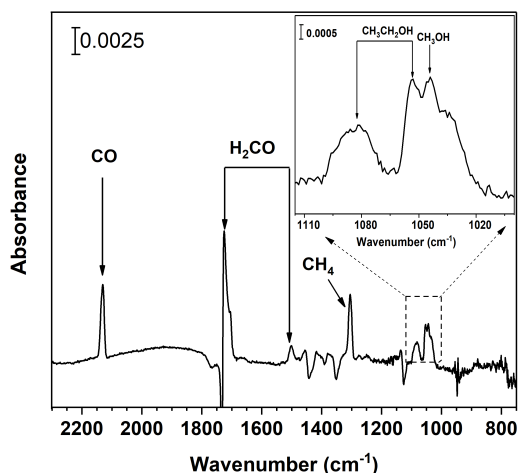
Finally, the presence of ketene ( $\text{H}_2\text{CCO}$ ) was also observed in our co-deposition experiments. We could not detect it in the IR because  $\text{H}_2\text{CCO}$  is easily hydrogenated (Ferrero et al. 2023), and its characteristic vibrational frequency (at  $2133 \text{ cm}^{-1}$ ) overlaps with the absorption of CO. However, clear evidence for the presence of  $\text{H}_2\text{CCO}$  in the reaction mixture was observed in our TPD experiments. The desorption peaks corresponding to  $m/z = 42$  and  $14$  at about  $75\text{--}90 \text{ K}$  and  $150\text{--}165 \text{ K}$  (Figure 11) can be derived from  $\text{H}_2\text{CCO}$  itself and its fragment (i.e.,  $\text{CH}_2$ ), respectively. The detection of these  $m/z = 14$  ( $\text{CH}_2$ ) and  $42$  ( $\text{H}_2\text{CCO}$ ) features in the TPD experiments, consistent with previous studies (Maity et al. 2015; Chuang et al. 2020; Fedoseev et al. 2022), provided strong evidence that  $\text{H}_2\text{CCO}$  was formed under the current experimental conditions, as supported by our theoretical models.

**Fig. 9.** TPD-QMS profile of pre-deposited  $\text{CH}_3\text{CHO}$  with H atoms (black line) comparable with  $\text{H}_2$  molecules (blue line) on c-ASW at 10 K:  $m/z = 16$  (top panel),  $m/z = 28$  (middle panel), and  $m/z = 46$  (bottom panel).

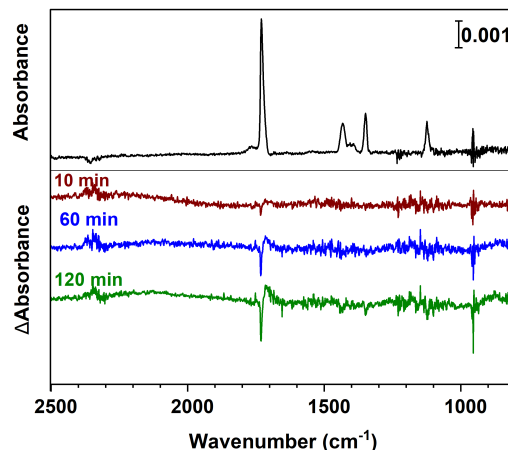
### 3.2.2. Isotopic labeling

Figure 12 shows the evolution of the difference spectra of  $\text{CH}_3\text{CHO}$  after exposure to D atoms for up to 2 hours as well as that of  $\text{CH}_3\text{CHO}$  without atomic exposure. Similar to the be-





**Fig. 10.** FTIR spectrum of codeposition of  $\text{CH}_3\text{CHO}$  and H atoms on Al at 10 K.



**Fig. 12.** Variation in the difference spectra of the solid  $\text{CH}_3\text{CHO}$  on the Al substrate at 10 K after exposure to D atoms for 10, 60, and 120 min comparable with the initial  $\text{CH}_3\text{CHO}$ .

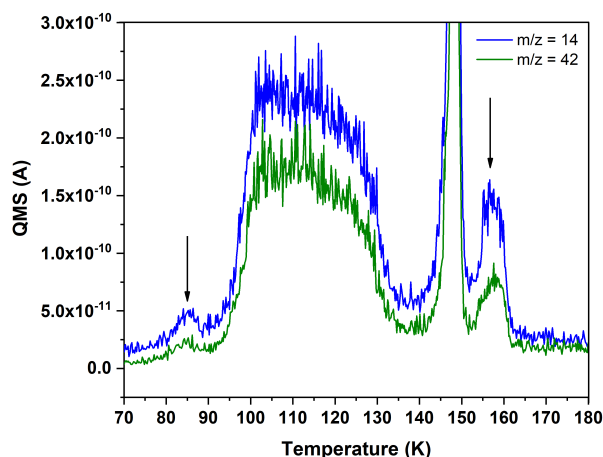


**Fig. 11.** TPD-QMS profile for the  $m/z = 14$  and  $42$ . Black arrows correspond to features attributable to  $\text{H}_2\text{CCO}$ , obtained after the reaction of the pre-deposited  $\text{CH}_3\text{CHO}$  with H atoms on c-ASW at 10K. The desorption peaks at 100–130 K and 140–150 K are derived from the remaining  $\text{CH}_3\text{CHO}$  on c-ASW after exposure to H atoms. The peaks at 75–90 K and 150–165 K represent the desorption of  $\text{H}_2\text{CCO}$  (Maity et al. 2015; Chuang et al. 2020; Fedoseev et al. 2022).

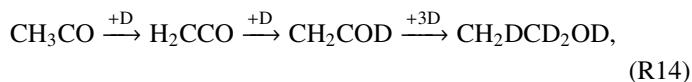
havior after exposure to H atoms, the C-O stretching band of  $\text{CH}_3\text{CHO}$  at  $1728\text{ cm}^{-1}$  decreased with exposure times, indicating the loss of  $\text{CH}_3\text{CHO}$  after interaction with D atoms on the Al substrate. Unfortunately, we cannot identify clear FTIR features for the products of the pre-deposited  $\text{CH}_3\text{CHO}$  with D atoms.

On the other hand, we observed various features for the formation of isotopologues of the products based on the TPD experiments. Figure 13 shows the TPD spectrum after the reaction of  $\text{CH}_3\text{CHO}$  with D atoms on Al substrate at 10 K. Since  $\text{CH}_3\text{CHO}$  desorbs at the temperature between 90 - 145 K and shows a CHO fragment ( $m/z = 29$ ) upon ionization, the desorption peak for  $m/z = 30$  (the CDO fragment) is attributed to the deuterated counterpart of acetaldehyde,  $\text{CH}_3\text{CDO}$ . Thus, the desorption peak ( $m/z = 30$  - top panel) observed at the same temperature after exposure to D atoms identified the formation of  $\text{CH}_3\text{CDO}$ . The formation of  $\text{CH}_3\text{CDO}$  provides compelling evidence for the re-

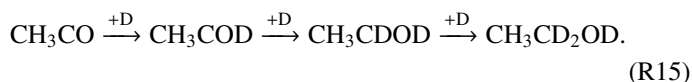
action between  $\text{CH}_3\text{CO}$  and D atoms:  $\text{CH}_3\text{CO} + \text{D} \rightarrow \text{CH}_3\text{CDO}$ . This process, in which the  $\text{CH}_3\text{CO}$  radical is produced by the reaction R6, is consistent with the calculated results.

Furthermore, the desorption peaks at  $m/z = 17$  and  $18$  (Figure 13 - middle and bottom panels) within the temperature range of 35 - 65 K were indicative of the formation of deuterated methane isotopologues,  $\text{CH}_3\text{D}$  and  $\text{CH}_2\text{D}_2$ . These species could be produced by the reactions in R16 as discussed in section 4.1, although we cannot be certain due to the high barriers associated with H abstraction in  $\text{CH}_3\text{D}$  (Lamberts et al. 2022).

A tiny peak corresponding to deuterated methanol ( $m/z = 36$ ;  $\text{CD}_3\text{OD}$ ) was observed to desorb at about 135 K (Figure 14). The formation of  $\text{CD}_3\text{OD}$  has been proposed to result from the deuteration of CO (Watanabe & Kouchi 2002), implying that the CO molecule is likely produced by the reaction of  $\text{CH}_3\text{CO}$  (reaction R11) with H or D atoms under the current experimental conditions, a finding consistent with our calculated results. In addition, we also observed the desorption peaks at  $m/z = 49$  and  $50$  in the temperature range of about 130 - 200 K. These peaks can be attributed to the formation of ethanol isotopologues corresponding to  $\text{CH}_3\text{CD}_2\text{OD}$  and/or  $\text{CH}_2\text{DCD}_2\text{OD}$  (see figure 15), which were obtained by reactions of  $\text{CH}_3\text{CO}$  radicals with D atoms, followed by:



and



The formation of ethanol isotopologues was consistent with the computational results obtained from reactions R9 and R10 (see section 3.1.3)

The appearance of a desorption peak observed at  $m/z = 48$  (see Figure 16) likely indicated the formation of  $\text{CH}_3\text{CHDOD}$ , resulting from the addition reaction of D to  $\text{CH}_3\text{CHO}$  under the current experimental conditions. Nevertheless, based on the

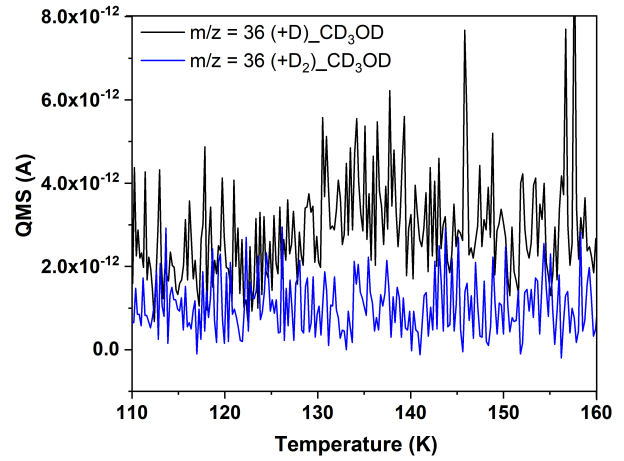
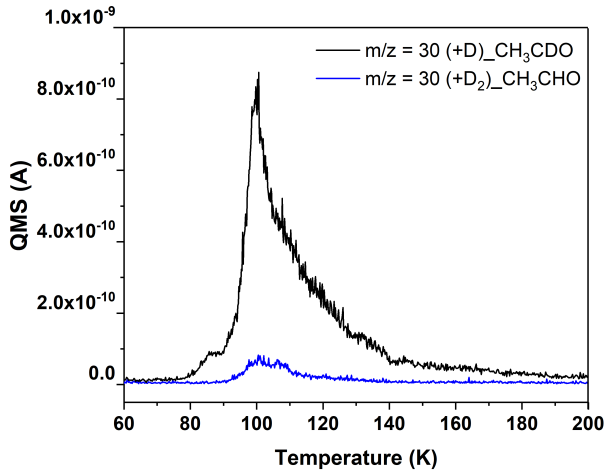


**Fig. 14.** TPD-QMS profile of  $m/z = 36$  observed for the pre-deposition of  $\text{CH}_3\text{CHO}$  and D atoms (black line) is compared with that of  $\text{D}_2$  molecules (blue line) on the Al substrate.

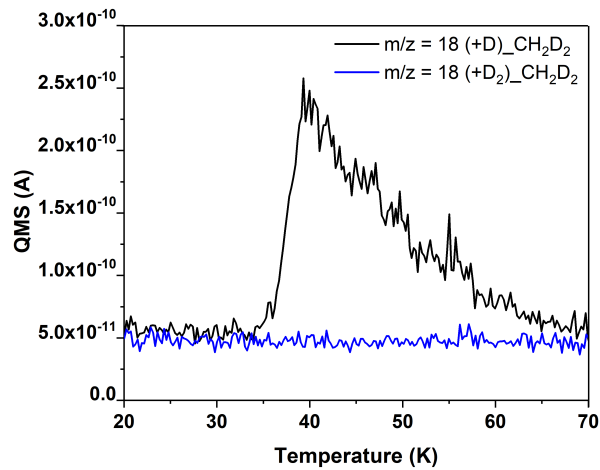
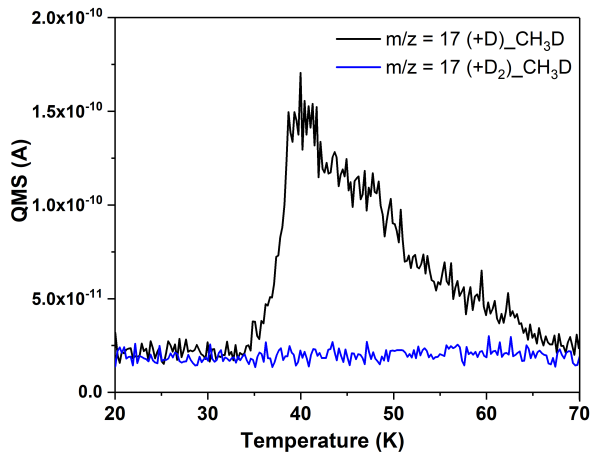


**Fig. 13.** TPD-QMS profile of pre-deposition of  $\text{CH}_3\text{CHO}$  with D atoms (black line) comparable with  $\text{D}_2$  (blue line) on Al substrate at 10 K,  $m/z = 30$  (top panel);  $m/z = 17$  (middle panel), and  $m/z = 18$  (bottom panel). The  $m/z = 30$  (top panel) in the blue line represents the fragmentation of  $\text{CH}_3\text{CHO}$ .

quantitative analysis of desorption areas for the reaction products,  $\text{CH}_3\text{CHDOD}$  was found to be a minor species in the reaction between  $\text{CH}_3\text{CHO}$  and D atoms. The predominant reaction

involved  $\text{CH}_3\text{CO}$  radicals with D atoms, leading a higher yield of different products.

## 4. Discussion

### 4.1. Merging theory and experiments: Comparison with previous works

Once the theoretical and experimental results are discussed we are in a privileged position to discuss the chemical mechanism behind the surface hydrogenation of acetaldehyde. The main experimental finding comes after the analysis of the 1432, 1349, and  $1124\text{ cm}^{-1}$  IR decay bands that, after comparison with the amount of deposited  $\text{CH}_3\text{CHO}$ , reveals a limited destruction of around of a 10%, with the rest of the  $\text{CH}_3\text{CHO}$  either unaffected or reformed after a H-abstraction and H-addition cycle. This finding is the easiest to rationalize based on the quantum chemical calculations. The limited destruction/conversion of  $\text{CH}_3\text{CHO}$  is due to the dominance of the R1 channel in the  $\text{CH}_3\text{CHO} + \text{H/D}$  reaction. Previous literature studies on the hydrogenation of aldehydes (Mondal et al. 2021) have not considered the H-abstraction reactions, perhaps in analogy to the limited importance of this type of reaction in the parent molecule formaldehyde,  $\text{H}_2\text{CO}$ . (Song & Kästner 2017). However, for  $\text{CH}_3\text{CHO}$  we found otherwise, with H-abstraction dominating the reactivity. Our deuteration experiments showed a tiny fraction of  $\text{CH}_3\text{CHDOD}$  indicating also the possibility of some hydrogen/deuterium addition in the hydrogenation/deuteration of  $\text{CH}_3\text{CHO}$ . This is somewhat coherent with the rate constants for H addition found in reactions R2 and R7, when  $\text{CH}_3\text{CHO}$  and H are in deep binding sites with slow diffusion rates (See Figure 6 and associated discussion). However, H-addition is a minor channel of the reaction, whose quantification to the total branching ratio is difficult. Therefore, in Section B we recommend considering a 1.0 branching ratio toward H-abstraction (Reaction R1).

After reaction R1, any subsequent hydrogenation on the new system involves the very reactive  $\text{CH}_3\text{CO}$  radical. From a theoretical standpoint, we determined that all reaction positions are, in principle, possible. Beginning with reaction R8, the H (or D) addition on this position reforms  $\text{CH}_3\text{CHO}$ , and based on the

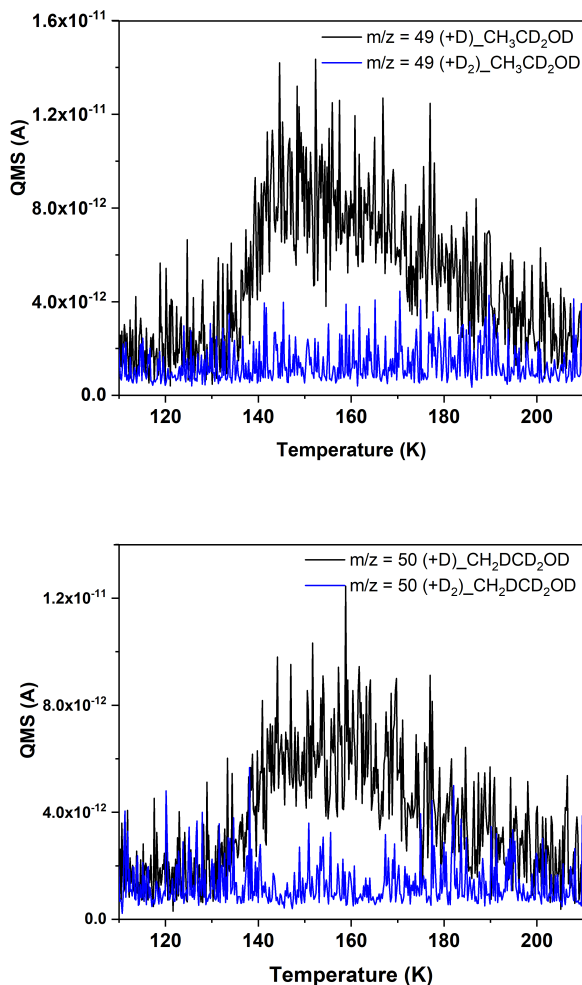


**Fig. 15.** TPD-QMS profiles of  $m/z = 49$  and  $50$  (black lines) desorbed at around 130 - 200 K, likely corresponding to ethanol isotopologues  $\text{CH}_3\text{CD}_2\text{OD}$  and/or  $\text{CH}_2\text{DCD}_2\text{OD}$ . These species were yielded through the reaction of  $\text{CH}_3\text{CHO}$  and D atoms, with behavior comparable to that of  $\text{D}_2$  molecules (blue line) on Al substrate at 10 K.

experiment, is the most likely outcome, with an 90 % of the reactive events in this direction, determined from the total fraction of  $\text{CH}_3\text{CHO}$  remaining after concluding our experiments. However, neither our calculations nor our experiments can rule out the contribution of the reforming of  $\text{CH}_3\text{CHO}$  from secondary reactions, i.e. hydrogenation of  $\text{H}_2\text{CCO}$  (see below and Ibrahim et al. 2022; Ferrero et al. 2023; Ibrahim et al. 2024). For reactions R9, R10 and R11 the products are  $\text{H}_2\text{CCO}$  (and  $\text{H}_2$ ),  $\text{CH}_3\text{COH}$  (methyl-methoxy carbene; Schreiner et al. (2011)), and  $\text{CH}_4 + \text{CO}$ . Beginning with  $\text{H}_2\text{CCO}$ , as we mention in Section 3.2, we cannot identify it in the IR spectrum because its main transition falls at  $2133\text{ cm}^{-1}$  overlapping with the CO band. However, the appearance of additional desorption features for  $m/z = 14$  ( $\text{CH}_2$ ) and  $42$  ( $\text{H}_2\text{CCO}$ ) between 75–90 K and 150–165 K in the TPD experiments (Figure 11) is in line with previous studies (Maity et al. 2015; Chuang et al. 2020; Fedoseev et al. 2022), which confirmed the desorption of  $\text{H}_2\text{CCO}$ . Nevertheless, Ferrero et al. (2023), using instanton calculations like the ones shown in this work, showed that the  $\text{H}_2\text{CCO}$  hydrogenation is very efficient with final products  $\text{CH}_3\text{CHO}$  and perhaps  $\text{C}_2\text{H}_5\text{OH}$  (ethanol). Bisschop et al. (2007); Ibrahim et al. (2022)

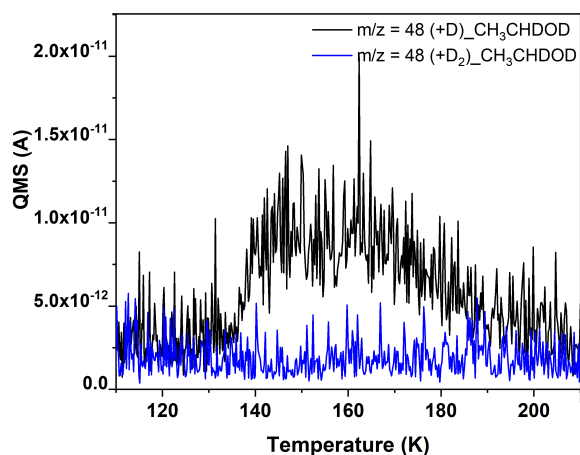
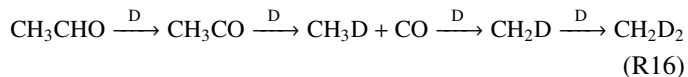


**Fig. 16.** TPD-QMS profile for the desorption peak observed at  $m/z = 48$  (black line) may be attributed to the formation of  $\text{CH}_3\text{CHDOD}$  through the addition reaction of D to  $\text{CH}_3\text{CHO}$ . This is in the comparison to the desorption behavior for  $\text{D}_2$  (blue line) on the Al substrate at 10 K.

also report  $\text{CO} + \text{CH}_4$  and  $\text{H}_2\text{CO}$  as products of the  $\text{H}_2\text{CCO} + \text{H}$  reaction, which is also coherent with our results. Combining experiments and theory, we determined that  $\text{H}_2\text{CCO}$  must be a product of the  $\text{CH}_3\text{CHO}$  hydrogenation under interstellar conditions, but in small amounts. Continuing with  $\text{CH}_3\text{COH}$ , even though it is formed in our calculations, we are unable to comment much on this species from an experimental point of view. This is due to the limited experimental data, but also to its transient nature. As a reactive carbene, we expect that the  $\text{CH}_3\text{COH} + 2\text{H} \rightarrow \text{C}_2\text{H}_5\text{OH}$  reaction will dominate in our experimental setup. Indeed,  $\text{C}_2\text{H}_5\text{OH}$  is seen in our co-deposition experiments, and the experimental and theoretical synergy carried out in this work allowed us that it is a secondary product of the hydrogenation of  $\text{CH}_3\text{CHO}$  rather than a direct one. The presence of  $\text{C}_2\text{H}_5\text{OH}$  was puzzling when checking the previous literature. In the experiments of Fedoseev et al. (2022) (for  $\text{H}_2\text{CCO} + \text{H}$ )  $\text{C}_2\text{H}_5\text{OH}$  was seen, as in our experiments. However, Ibrahim et al. (2022) and Ibrahim et al. (2024) do not report its presence after the same reaction. The reason for this disagreement is likely due to the experimental conditions, and our results provide a reconciling scenario. We could not detect  $\text{C}_2\text{H}_5\text{OH}$  using the IR spectra in our pre-deposition experiment, which would be the one directly comparable to the experiments of Ibrahim et al. (2022) needing to rely on TPD-QMS measurements (See Figure 9) for that. However, the presence of  $\text{C}_2\text{H}_5\text{OH}$  was seen in our co-deposition experiments starting from  $\text{CH}_3\text{CHO}$  mimicking Fedoseev et al. (2022). Although other experimental conditions differ between our setups, like H flux or irradiation time, we think the reason for the disagreement stems from the deposition strategy.

Finally, the last experimental product that we observe is  $\text{CH}_4$  (and its isotopologues, see below) and  $\text{CO}$ . Given the enormous  $\Delta H^\ddagger$  found for reaction R5, the formation of  $\text{CH}_4$  must come from the hydrogenation of  $\text{CH}_3\text{CO}$ , or perhaps of further radicals in the hydrogenation sequence of  $\text{CH}_3\text{CO}$ , out of the scope of the present paper. However, we find it likely that  $\text{CH}_4$  comes directly from  $\text{CH}_3\text{CO}$  via reaction R11.  $\text{CO}$  was seen in our experiments, either directly as  $\text{CO}$  or as its hydrogenated products  $\text{H}_2\text{CO}$  and  $\text{CH}_3\text{OH}$  as discussed above.

Our deuteration experiments do show a variety of isotopologues of the products discussed in the previous paragraphs. The presence or absence of certain isotopologues not only aids our experiments but also allows us to confirm our theoretical observations. For  $\text{CH}_3\text{CHO} + \text{D}$  our experiments reveal the majoritarian formation of  $\text{CH}_3\text{CO}$  that later reforms  $\text{CH}_3\text{CDO}$ . Likewise, we clearly see the formation of  $\text{CH}_3\text{D}$  and  $\text{CH}_2\text{D}_2$ , that might arise from the sequence of reactions (omitting HD when applicable):



These reactions serve as a proxy to suggest that the  $\text{CH}_3\text{D} + \text{H/D} \longrightarrow \text{CH}_2\text{D} + \text{H}_2/\text{HD}$  could be a viable reaction, although we cannot confidently ensure it, because some reaction steps in R16 have high barriers. A preliminary search at the rev-DSD-PBEP86(D4)/jun-cc-pV(T+d)Z level for the  $\text{CH}_3\text{D} + \text{D} \longrightarrow \text{CH}_2\text{D} + \text{HD}$  (The third reaction in the scheme of reactions shown in R16) shows that the reaction is slightly exothermic, unlike the full hydrogenated counterpart, by  $\Delta H^{\text{R}} = -3.3 \text{ kJ mol}^{-1}$  (-404 K), making the reaction scheme R16 in principle viable albeit probably very slow. Overall, while the presence of  $\text{CH}_3\text{D}$  is easy to explain from experiments and theory, the presence of  $\text{CH}_2\text{D}_2$  is not that easily explained, with secondary and tertiary hydrogenation branches being important, and requiring a careful validation out of the scope of this work. The CO formed in the previous reaction can also be hydrogenated to fully deuterated methanol ( $\text{CD}_3\text{OD}$ ) (Watanabe & Kouchi 2002), a reaction that could not happen without the formation of CO, further increasing our confidence in the viability of reaction R11. We also observe clear signals of the formation of ethanol isotopologues, especially of  $\text{CH}_3\text{CD}_2\text{OD}$  or  $\text{CH}_2\text{DCD}_2\text{OD}$  (Reaction scheme in R14 and R15 and Figure 15), merging once again experimental and theoretical results and highlighting the importance of reaction R1 as the initiator of the complex chemistry observed in the experiments. We reiterate that a small fraction of  $\text{CH}_3\text{CHDOD}$  was also found (Figure 16).

We briefly comment on the differences between our new set of experiments and the classical ones of Bisschop et al. (2007), that inspired this work. In both our experiments we obtain the same products of the reaction, although in different proportions. While we only find a conversion of  $\text{CH}_3\text{CHO}$  equal to 10% in the duration of our experiment, Bisschop et al. (2007) reports variable conversion rates varying between 30% to almost total conversion (See their Table 5). These quantitative differences should come from different factors, being the most likely reasons the temperature of the H atoms and the selection of substrate. In our setup, the H atoms are cooled down before hitting the surface, guaranteeing immediate thermalization on the surface. In Bisschop et al. (2007) the H-atoms were introduced in the chamber at 300 K, which can promote a plethora of reactions through different reaction mechanisms like the Eley-Rideal or Harris-Kasemo ones. Moreover, in our setup, we carry our experiments on ASW where the interactions between  $\text{CH}_3\text{CHO}$  molecules with the surface will be different than in pure  $\text{CH}_3\text{CHO}$  or in a metallic substrate.

Lastly, in light of what it has been presented in this section we have prepared a series of recommendations to include this reaction in astrochemical rate equation models. We have gathered our conclusions in Appendix B.

## 4.2. Astrophysical Implications

Our results carry a series of implications for the astrochemical community, in particular regarding the deuteration and reactive desorption of  $\text{CH}_3\text{CHO}$ . Acetaldehyde is a molecule routinely detected in a variety of interstellar environments (Cazaux et al. 2003; Occhiogrosso et al. 2014; Walsh et al. 2014; Imai et al. 2016; Codella et al. 2015; Holdship et al. 2019; Bonfand et al. 2019), including several detections in prestellar cores (Bacmann et al. 2012; Cernicharo et al. 2012; Scibelli et al. 2021; Jiménez-Serra et al. 2016; Megías et al. 2022), where there is little energy for bringing the molecules to the gas phase, where they are detected. The formation of  $\text{CH}_3\text{CHO}$  is debated, including the gas-phase route  $\text{C}_2\text{H}_5 + \text{O} \longrightarrow \text{CH}_3\text{CHO} + \text{H}$  (Vazart et al. 2020) or ice surface routes. These routes involve the radical-radical recombination of  $\text{HCO} + \text{CH}_3$ , on ice (Garrod 2013; Molpeceres et al. 2024a; Lamberts et al. 2019) although on water ice this route is sometimes considered less effective (Enrique-Romero et al. 2021). Alternative routes include the radiolytic (Shingledecker et al. 2018) or non-thermal formation (Jin & Garrod 2020). Regardless of the formation route,  $\text{CH}_3\text{CHO}$  will form or deplete on the grain, and it is at this stage when the title reaction can take place.

Our results show that acetaldehyde is mostly processed and reformed through reactions R1 and R8, and although other products and routes exist, as extensively discussed in this manuscript, the astrophysical implications of our work are mainly carried by this limited destruction, and we will focus on those in this section. In the first place, we talk about reactive desorption. When an H atom is abstracted from the HCO moiety in  $\text{CH}_3\text{CHO}$ , the hydrogenation of the resulting  $\text{CH}_3\text{CO}$  radical could trigger a chemical desorption event, considering that the binding energy of  $\text{CH}_3\text{CHO}$  is among the lowest for COMs. As we indicated in Section 3.2 we cannot confirm this possibility, as the different hydrogenation branches opened from our reaction make it very difficult to confirm or deny the possibility of chemical desorption. Optimistic estimates of the probability of chemical desorption for COMs place the probability per reaction event at around 1% (Garrod et al. 2007). Because this amount should be included in the 10% of nonreformed  $\text{CH}_3\text{CHO}$  it is experimentally extremely hard to prove. Yet,  $\text{CH}_3\text{CHO}$  constitutes the best-case scenario with an effective H-abstraction / H-Addition cycle, the high reaction energy for the  $\text{CH}_3\text{CO} + \text{H}$  reaction and the relatively low binding energy on water ice (Molpeceres et al. 2022b; Ferrero et al. 2022).

Another important implication of our work pertains to the formation of ethanol,  $\text{C}_2\text{H}_5\text{OH}$ , which is predicted to be formed in very low amounts from reaction R2, but actually from the evolution of the  $\text{CH}_3\text{CO} + \text{H}$  reaction. This is in contrast with the hydrogenation of formaldehyde ( $\text{H}_2\text{CO}$ ), the prototypical interstellar aldehyde, that leads to methanol  $\text{CH}_3\text{OH}$  (Watanabe & Kouchi 2002; Hidaka et al. 2004). In Mondal et al. (2021) the authors indicate that the connection from  $\text{CH}_3\text{CHO}$  with  $\text{C}_2\text{H}_5\text{OH}$  through direct hydrogenation is not enough to account for the abundances of  $\text{C}_2\text{H}_5\text{OH}$  in the hot core G10.47+0.03, and that their models revealed that  $\text{CH}_3 + \text{CH}_2\text{OH} \longrightarrow \text{C}_2\text{H}_5\text{OH}$  is needed to explain the observations. Our results fully adhere to this picture and strongly suggest that the link between  $\text{CH}_3\text{CHO}$  and  $\text{C}_2\text{H}_5\text{OH}$  is not straightforward.

Finally, we reserve some words for the possibility of finding deuterated acetaldehyde. A relatively recent publication Jørgensen et al. (2018) showed that  $\text{CH}_3\text{CDO}$  is the isotopologue of a COM with the highest ratio to the non-deuterated molecule, with a percentage of 8% in IRAS16293–2422. This result rein-

forces the results obtained in this work and suggests as a possible explanation for this observation the H-abstraction / H-addition route discussed in this work, in addition to the explicit detection of CH<sub>3</sub>CDO in our experiments. Nevertheless, it is important to remark that other CH<sub>3</sub>CHO isotopologues CH<sub>2</sub>DCHO and CD<sub>2</sub>HCHO have also been detected in the same source (Coudert et al. 2019; Ferrer Asensio et al. 2023). These last findings do not rule out the importance of our reaction routes but show the complexity associated with deuterium fractionation in the ISM, where gas and surface chemistry are in constant interplay.

## 5. Conclusions

We conclude by providing a series of bullet points that summarize our work.

1. Our calculations and experiments show that the CH<sub>3</sub>CHO + H does not lead to significant conversion. The reason for that limited conversion is found in the dominance of hydrogen abstraction in the HCO moiety of CH<sub>3</sub>CHO which in turn leads to facile reforming of CH<sub>3</sub>CHO. Quantifying this conversion leads us to a maximum of 10% of CH<sub>3</sub>CHO under our experimental conditions.
2. Other minor products of the reaction of CH<sub>3</sub>CHO with H come from the hydrogenation of the CH<sub>3</sub>CO reactive radical and are H<sub>2</sub>CO, CH<sub>3</sub>OH, C<sub>2</sub>H<sub>5</sub>OH, H<sub>2</sub>CCO, CO or CH<sub>4</sub> revealing a very complex chemistry. In general, our calculations and previous knowledge of the chemistry of the different intermediates found in our calculations can satisfactorily explain the different products that we obtain. However, and because the study of the CH<sub>3</sub>CO + H is more qualitative due to theoretical constraints, more sophisticated approaches are required to derive accurate branching ratios for the reaction.
3. Our experiments reveal the effective formation of CH<sub>3</sub>CDO supporting the idea of a H/D-abstraction and H/D-addition cycle as the major route for the CH<sub>3</sub>CHO + H reaction.
4. Although we can explain the vast majority of our experimental observations with our calculations, the presence of doubly deuterated methane CH<sub>2</sub>D<sub>2</sub> and the CH<sub>3</sub>CHDOD isotopologue in our deuteration experiments remains difficult to explain. In general, several hydrogenation and deuteration branches of the minor products could lead to different products making explaining the complete reaction network an unbearable task.
5. Our results align with the results found in the modeling literature (Mondal et al. 2021) suggesting that the link between acetaldehyde and ethanol is not direct from the former to the latter via hydrogenation.
6. We were unable to determine whether reactive desorption happens for CH<sub>3</sub>CHO although in light of the energetic parameters found by our theoretical calculations, summed to the H-abstraction and addition cycle present in the reaction, we consider it a likely outcome.
7. Our experiments and calculations nicely explain the excess of CH<sub>3</sub>CDO found in the IRAS16293–2422 hot core (Jørgensen et al. 2018). However, we remark that a single chemical reaction is not enough to explain complex deuterium enrichment processes in space.

Future avenues of the present work could address the presence of certain non-easy-to-explain isotopologues in our experiments, or the study of the impact of the here-derived quantities in realistic astrochemical models. Likewise, we are currently tackling the complex problem of CH<sub>3</sub>CHO chemical desorption

using more sophisticated molecular dynamics approaches. We will continue combining experiments and calculations to fully unravel complex interstellar reaction networks.

*Acknowledgements.* The authors thank the anonymous reviewer for the thorough revision of the manuscript. We thank Professor Johannes Kästner at Stuttgart University for providing a development version of CHEMShell. We also thank Dr. Masashi Tsuge and Dr. Hiroshi Hidaka for fruitful discussions on the experimental results. G.M. acknowledges the support of the grant RYC2022-035442-I funded by MICIU/AEI/10.13039/501100011033 and ESF+. G.M. also received support from project 20245AT016 (Proyectos Intramurales CSIC). We acknowledge the computational resources provided by bwHPC and the German Research Foundation (DFG) through grant no INST 40/575-1 FUGG (JUSTUS 2 cluster), the DRAGO computer cluster managed by SGAI-CSIC, and the Galician Supercomputing Center (CESGA). The supercomputer FinisTerra III and its permanent data storage system have been funded by the Spanish Ministry of Science and Innovation, the Galician Government and the European Regional Development Fund (ERDF). Y.O. and N.W. acknowledge the funding support from JSPS KAKENHI grant nos. JP23H03980, JP21H04501, and JP22H00159.

## References

- Alvarez-Barcia, S., Russ, P., Kästner, J., & Lamberts, T. 2018, *Monthly Notices of the Royal Astronomical Society*, 479, 2007, arXiv: 1806.02062
- Asgeirsson, V., Jónsson, H., & Wikfeldt, K. T. 2017, *Journal of Physical Chemistry C*, 121, 1648
- Bacmann, A. & Faure, A. 2014, in SF2A-2014: Proceedings of the Annual meeting of the French Society of Astronomy and Astrophysics, ed. J. Ballet, F. Martins, F. Bournaud, R. Monier, & C. Reylé, 3–8
- Bacmann, A., Taquet, V., Faure, A., Kahane, C., & Ceccarelli, C. 2012, *Astronomy & Astrophysics*, 541, L12
- Barone, V. & Cossi, M. 1998, *The Journal of Physical Chemistry A*, 102, 1995
- Bartlett, R. J. & Purvis, G. D. 1978, *International Journal of Quantum Chemistry*, 14, 561
- Bennett, C. J., Jamieson, C. S., Osamura, Y., & Kaiser, R. I. 2005, *ApJ*, 624, 1097
- Bisschop, S. E., Fuchs, G. W., van Dishoeck, E. F., & Linnartz, H. 2007, *Astron. Astrophys.*, 474, 1061
- Bohlin, R. C., Savage, B. D., & Drake, J. F. 1978, *The Astrophysical Journal*, 224, 132
- Bonfand, M., Belloche, A., Garrod, R. T., et al. 2019, *Astronomy & Astrophysics*, 628, A27
- Caldeweyher, E., Ehlert, S., Hansen, A., et al. 2019, *Journal of Chemical Physics*, 150
- Cazaux, S., Tielens, A. G. G. M., Ceccarelli, C., et al. 2003, *Astrophys. J.*, 593, L51
- Ceccarelli, C., Caselli, P., Bockelée-Morvan, D., et al. 2014, in *Protostars and Planets VI*, ed. H. Beuther, R. S. Klessen, C. P. Dullemond, & T. Henning, 859–882
- Cernicharo, J., Marcelino, N., Roueff, E., et al. 2012, *The Astrophysical Journal*, 759, L43
- Chang, Q., Cuppen, H. M., & Herbst, E. 2007, *Astronomy & Astrophysics*, 469, 973
- Chuang, K. J., Fedoseev, G., Ioppolo, S., van Dishoeck, E. F., & Linnartz, H. 2020, *Monthly Notices of the Royal Astronomical Society: Letters*, 455, 1702
- Codella, C., Fontani, F., Ceccarelli, C., et al. 2015, *Mon. Not. R. Astron. Soc. Lett.*, 449, L11
- Coudert, L. H., Margulès, L., Vastel, C., et al. 2019, *Astronomy & Astrophysics*, 624, A70
- Dunning, T. H. 1989, *The Journal of Chemical Physics*, 90
- Eckart, C. 1930, *Physical Review*, 35, 1303, publisher: American Physical Society ISBN: 0031-899X
- Enrique-Romero, J., Ceccarelli, C., Rimola, A., et al. 2021, *Astronomy & Astrophysics*, 655, A9
- Enrique-Romero, J., Rimola, A., Ceccarelli, C., et al. 2022, *The Astrophysical Journal Supplement Series*, 259, 39
- Fedoseev, G., Qasim, D., Chuang, K.-J., et al. 2022, *ApJ*, 924, 110
- Ferrer Asensio, J., Spezzano, S., Coudert, L. H., et al. 2023, *Astronomy & Astrophysics*, 670, A177
- Ferrero, S., Ceccarelli, C., Ugliengo, P., Sodupe, M., & Rimola, A. 2023, *The Astrophysical Journal*, 951, 150
- Ferrero, S., Grieco, F., Ibrahim Mohamed, A.-S., et al. 2022, *Monthly Notices of the Royal Astronomical Society*, 516, 2586
- Fuchs, G. W., Cuppen, H. M., Ioppolo, S., et al. 2009, *Astronomy and Astrophysics*, 505, 629
- García-Ratés, M. & Neese, F. 2020, *Journal of Computational Chemistry*, 41, 922

- Garrod, R. T. 2013, *Astrophys. J.*, 765, 60
- Garrod, R. T., Jin, M., Matis, K. A., et al. 2022, *The Astrophysical Journal Supplement Series*, 259, 1
- Garrod, R. T., Wakelam, V., & Herbst, E. 2007, *Astronomy & Astrophysics*, 467, 1103
- Gerakines, P. A., Schutte, W. A., Greenberg, J. M., & van Dishoeck, E. F. 1995, *A&A*, 296, 810
- Gillan, M. J. 1987, *Journal of Physics C: Solid State Physics*, 20, 3621, publisher: IOP Publishing
- Guo, Y., Riplinger, C., Becker, U., et al. 2018, *The Journal of Chemical Physics*, 148, 011101
- Herbst, E. & Van Dishoeck, E. F. 2009, *Annual Review of Astronomy and Astrophysics*, 47, 427, publisher: Annual Reviews ISBN: 0066-4146
- Hidaka, H., Watanabe, N., Shiraki, T., Nagaoka, A., & Kouchi, A. 2004, *ApJ*, 614, 1124
- Holdship, J., Viti, S., Codella, C., et al. 2019, *Astrophys. J.*, 880, 138
- Hudson, R. L. 2017, *Spectrochimica Acta Part A: Molecular Spectroscopy*, 187, 82
- Ibrahim, M., Guillemin, J.-C., Chaquin, P., Markovits, A., & Krim, L. 2022, *Physical Chemistry Chemical Physics*, 24, 23245
- Ibrahim, M., Guillemin, J.-C., Chaquin, P., Markovits, A., & Krim, L. 2024, *Physical Chemistry Chemical Physics*, 26, 4200
- Imai, M., Sakai, N., Oya, Y., et al. 2016, *Astrophys. J.*, 830, L37
- Jiménez-Serra, I., Vasyunin, A. I., Caselli, P., et al. 2016, *ApJ*, 830, L6
- Jiménez-Serra, I., Vasyunin, A. I., Spezzano, S., et al. 2021, *The Astrophysical Journal*, 917, 44
- Jiménez-Serra, I., Vasyunin, A. I., Caselli, P., et al. 2016, *The Astrophysical Journal*, 830, L6, arXiv: 1609.05045 Publisher: American Astronomical Society
- Jin, M. & Garrod, R. T. 2020, *The Astrophysical Journal Supplement Series*, 249, 26, arXiv: 2006.11127 Publisher: American Astronomical Society
- Jørgensen, J. K., Müller, H. S. P., Calcutt, H., et al. 2018, *Astronomy & Astrophysics*, 620, A170
- Kästner, J. 2014, *Wiley Interdisciplinary Reviews: Computational Molecular Science*, 4, 158
- Kästner, J., Carr, J. M., Keal, T. W., et al. 2009, *J. Phys. Chem. A*, 113, 11856
- Knowles, P. J., Hampel, C., & Werner, H.-J. 1993, *The Journal of Chemical Physics*, 99, 5219
- Kozuch, S. & Martin, J. M. 2011, *Physical Chemistry Chemical Physics*, 13, 20104, publisher: The Royal Society of Chemistry
- Lamberts, T. 2018, *Astronomy and Astrophysics*, 615, L2
- Lamberts, T., Fedoseev, G., Van Hemert, M. C., et al. 2022, *The Astrophysical Journal*, 928, 48
- Lamberts, T. & Kästner, J. 2017a, *The Astrophysical Journal*, 846, 43, arXiv: 1708.05555 Publisher: IOP Publishing
- Lamberts, T. & Kästner, J. 2017b, *Journal of Physical Chemistry A*, 121, 9736, publisher: American Chemical Society
- Lamberts, T., Markmeyer, M. N., Kolb, F. J., & Kästner, J. 2019, *ACS Earth and Space Chemistry*, 3, 958
- Maity, S., Kaiser, R. I., & Jones, B. M. 2015, *Physical Chemistry Chemical Physics*, 17, 3081
- Megías, A., Jiménez-Serra, I., Martín-Pintado, J., et al. 2022, *Monthly Notices of the Royal Astronomical Society*, 519, 1601
- Meisner, J., Lamberts, T., & Kästner, J. 2017, *ACS Earth and Space Chemistry*, 1, 399, arXiv: 1708.05559 Publisher: American Chemical Society
- Metz, S., Kästner, J., Sokol, A. A., Keal, T. W., & Sherwood, P. 2014, *Wiley Interdisciplinary Reviews: Computational Molecular Science*, 4, 101
- Miksch, A. M., Riffelt, A., Oliveira, R., Kästner, J., & Molpeceres, G. 2021, *Monthly Notices of the Royal Astronomical Society*, 505, 3157
- Molpeceres, G., Furuya, K., & Aikawa, Y. 2024a, *Astronomy & Astrophysics*, 688, A150
- Molpeceres, G., Jimenez-Serra, I., Oba, Y., et al. 2022a, *Astronomy & Astrophysics*, 663
- Molpeceres, G. & Kästner, J. 2021, *The Astrophysical Journal*, 910, 55
- Molpeceres, G., Kästner, J., Herrero, V. J., Peláez, R. J., & Maté, B. 2022b, *Astronomy & Astrophysics*, 664, A169
- Molpeceres, G. & Rivilla, V. M. 2022, *Astronomy & Astrophysics*, 665, A27
- Molpeceres, G., Rivilla, V. M., Furuya, K., et al. 2023, *Monthly Notices of the Royal Astronomical Society*, 521, 6061
- Molpeceres, G., Tsuge, M., Furuya, K., et al. 2024b, *The Journal of Physical Chemistry A*, acs.jpca.3c08286
- Mondal, S. K., Gorai, P., Sil, M., et al. 2021, *The Astrophysical Journal*, 922, 194
- Nagaoka, A., Watanabe, N., & Kouchi, A. 2007, *The Journal of Physical Chemistry A*, 111, 3016
- Neese, F., Wennmohs, F., Becker, U., & Riplinger, C. 2020, *Journal of Chemical Physics*, 152, 224108
- Nguyen, T., Fourré, I., Favre, C., et al. 2019, *Astronomy & Astrophysics*, 628, A15
- Nguyen, T., Oba, Y., Sameera, W. M. C., et al. 2023, *ApJ*, 944, 219
- Nguyen, T., Oba, Y., Sameera, W. M. C., Kouchi, A., & Watanabe, N. 2021a, *ApJ*, 918, 73
- Nguyen, T., Oba, Y., Sameera, W. M. C., Kouchi, A., & Watanabe, N. 2021b, *ApJ*, 922, 146
- Nguyen, T., Oba, Y., Shimonishi, T., Kouchi, A., & Watanabe, N. 2020, *ApJ*, 898, L52
- Oba, Y., Osaka, K., Watanabe, N., Chigai, T., & Kouchi, A. 2014, *FaDi*, 168, 185
- Oba, Y., Tomaru, T., Lamberts, T., Kouchi, A., & Watanabe, N. 2018, *Nature Astronomy*, 2, 228
- Occhiogrosso, A., Vasyunin, A., Herbst, E., et al. 2014, *Astronomy & Astrophysics*, 564, A123
- Papajak, E., Zheng, J., Xu, X., Leverentz, H. R., & Truhlar, D. G. 2011, *Journal of Chemical Theory and Computation*, 7, 3027
- Perrero, J., Ugliengo, P., Ceccarelli, C., & Rimola, A. 2023, *MNRAS*, 525, 2654
- Purvis, G. D. & Bartlett, R. J. 1982, *The Journal of Chemical Physics*, 76, 1910
- Qasim, D., Fedoseev, G., Chuang, K. J., et al. 2020, *Nature Astronomy*, 4, 781, arXiv: 2004.02506
- Rimola, A., Taquet, V., Ugliengo, P., Balucani, N., & Ceccarelli, C. 2014, *Astronomy and Astrophysics*, 572
- Rommel, J. B., Goumans, T. P., & Kästner, J. 2011, *J. Chem. Theory Comp.*, 7, 690
- Santra, G., Sylvetsky, N., & Martin, J. M. L. 2019, *The Journal of Physical Chemistry A*, 123, 5129
- Schreiner, P. R., Reisenauer, H. P., Ley, D., et al. 2011, *Science*, 332, 1300
- Scibelli, S., Shirley, Y., Vasyunin, A., & Launhardt, R. 2021, *Mon. Not. Royal Astron. Soc.*, 504, 5754
- Senevirathne, B., Andersson, S., Dulieu, F., & Nyman, G. 2017, *Molecular Astrophysics*, 6, 59
- Shingledecker, C. N., Tennis, J., Gal, R. L., & Herbst, E. 2018, *The Astrophysical Journal*, 861, 20
- Simons, M. A., Lamberts, T., & Cuppen, H. M. 2020, *Astronomy and Astrophysics*, 634, A52, arXiv: 2001.04895
- Song, L. & Kästner, J. 2017, *The Astrophysical Journal*, 850, 118
- Truong, T. N. & Stefanovich, E. V. 1995, *Chemical Physics Letters*, 240, 253
- Vazart, F., Ceccarelli, C., Balucani, N., Bianchi, E., & Skouteris, D. 2020, *Monthly Notices of the Royal Astronomical Society*, 499, 5547
- Walsh, C., Millar, T. J., Nomura, H., et al. 2014, *Astronomy & Astrophysics*, 563, A33
- Watanabe, N. & Kouchi, A. 2002, *ApJ*, 571, L173
- Watanabe, N., Nagaoka, A., Hidaka, H., et al. 2006, *P&SS*, 54, 1107, simulations in Laboratory
- Woon, D. E. & Dunning, T. H. 1994, *The Journal of Chemical Physics*, 100, 2975, publisher: American Institute of Physics ISBN: 0021-9606

**Table A.1.** Comparison in activation energies for the reactions R1-R5 using a gas phase ( $\Delta H_{\text{Gas}}^{\ddagger}$  in  $\text{kJ mol}^{-1}$ ) and an explicit two  $\text{H}_2\text{O}$  model ( $\Delta H_{2\text{H}_2\text{O}}^{\ddagger}$  in  $\text{kJ mol}^{-1}$ ).

Reaction	Label	$\Delta H_{\text{Gas}}^{\ddagger}$	$\Delta H_{2\text{H}_2\text{O}}^{\ddagger}$
$\text{CH}_3\text{CHO} + \text{H} \longrightarrow \text{CH}_3\text{CO} + \text{H}_2$	R1	18.5	19.6
$\text{CH}_3\text{CHO} + \text{H} \longrightarrow \text{CH}_3\text{CH}_2\text{O}$	R2	31.0	27.7
$\text{CH}_3\text{CHO} + \text{H} \longrightarrow \text{CH}_2\text{CHO} + \text{H}_2$	R3	41.2	37.1
$\text{CH}_3\text{CHO} + \text{H} \longrightarrow \text{CH}_3\text{CHOH}$	R4	47.3	48.1
$\text{CH}_3\text{CHO} + \text{H} \longrightarrow \text{CH}_4 + \text{HCO}$	R5	142.6	140.1

## Appendix A: Determination of reaction barriers using a small $2\text{H}_2\text{O}$ cluster model. Validity of the implicit surface approximation.

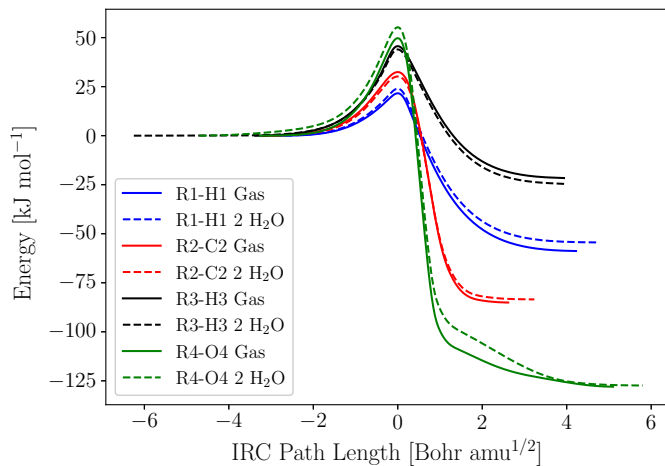


**Fig. A.1.** Equivalent to Figure 2, but including reactions using an explicit  $2\text{H}_2\text{O}$  model (dashed line).

In the main text, we obtain the reaction descriptors and subsequent kinetic rate constants using two implicit approximations. In addition to an implicit solvation approach, we assume that the ASW surface does not play a major role in the reaction, introducing surface effects *via* rotational partition function fixing. These approximations are required for including nuclear quantum effects in the calculation of our rate constant while keeping an accurate potential (CCSD(T)/aug-cc-pVTZ//rev-DSD-PBEP86(D4)/jun-cc-pv(T+d)Z). The applicability of these approximations is ensured by a single condition, that the reaction descriptors are not affected by the water matrix. Such a condition is fulfilled normally in adsorbates bound to ASW *via* weak physisorption forces, although it has been applied to molecules as tightly bound as OH (Meisner et al. 2017; Lamberts & Kästner 2017a,b; Molpeceres & Kästner 2021; Molpeceres et al. 2022a; Molpeceres & Rivilla 2022; Ferrero et al. 2023). Acetaldehyde has one of the lowest binding energies found for any COM (Ferrero et al. 2022; Molpeceres et al. 2022b) so we do not expect a different behavior to the cases cited above. Nevertheless, we explicitly tested whether the introduction of explicit water affects the reaction descriptors and reaction profiles in our studied reactions. The tests we performed include comparing the activation energies, with and without water molecules,  $\Delta H_{\text{Gas}}^{\ddagger}$ , and

$\Delta H_{2\text{H}_2\text{O}}^{\ddagger}$ . For the  $2\text{H}_2\text{O}$  coupled cluster calculations, we used the domain local pair natural orbital (DLPNO) (Guo et al. 2018) version of CCSD(T), using a TightPNO localization scheme.

The results of the tests are shown in Figure A.1 and Table A.1. Starting with the IRC profiles shown in Figure A.1 it is evident that in all cases the barrier shapes are almost identical, with subtle differences. These are, for example, that in the  $2\text{H}_2\text{O}$  model the IRC path extends beyond the gas phase one, a consequence of the interaction of the reacting molecules with the  $2\text{H}_2\text{O}$ . The most important deviation appears for reaction R4 that, in the  $2\text{H}_2\text{O}$  model, experiences a restructuring of the water dimer to better accommodate the  $\text{CH}_2\text{CHO}$  radical. Nevertheless, the change in the profile is still very small. Similarly, the deviations in  $\Delta H^{\ddagger}$  are minimal and cannot be ruled out if the deviations are a consequence of the  $2\text{H}_2\text{O}$  model or by the DLPNO scheme used in the computation of the molecular energies. Overall, we find that including explicit water molecules does not affect our results. While the inclusion of further water molecules can also have an impact, this impact will not be larger than the one exerted by the closest water molecules. We remember that polar solvent effects are introduced in the main text utilizing an implicit solvation approach. Overall, we confidently conclude that the approximations in this work are justified in light of these results.

## Appendix B: Modeling recommendations

The picture left by the combination of our calculations and experiments is a complex one, despite the relative simplicity of the  $\text{CH}_3\text{CHO}$  molecule. We think this is a trait common to all COMs (with more than one carbon atom) hydrogenations. As chemical complexity increases, the possibility of reaction branches starts to emerge, and hydrogenation experiments are harder to reconcile with theory because the former are suited to detect final products whereas the latter are more suited to investigate elementary processes. We feel that approaches like ours, merging experiments and theory are fundamental to securely identify representative interstellar reaction routes.

However, the here studied reactions (or reaction schemes) seek to provide reliable data to feed astrochemical models, and in the particular case of this study, COMs and deuterium fractionation reaction networks, aiming to a better description of interstellar environments. Once the complexity of a reaction scheme starts to increase, as the one shown in this work, several assumptions and recommendations for astrochemical models need to be given. In this section we provide our guidelines for the treatment of  $\text{CH}_3\text{CHO}$  hydrogenation, justifying our decisions.<sup>5</sup> In the first place, and although the most exact approach is to include the exact rate constants for R2-R4 and an accurate modeling of H atom diffusion, we consider safe deactivating the reactions in reaction networks. We base our recommendation on the limited conversion that we observe for  $\text{CH}_3\text{CHO}$ , which remains mostly unaltered in our experiments, an observation supported by the  $\text{CH}_3\text{CHO} \rightleftharpoons \text{CH}_3\text{CO} + \text{H}$  cycle that we derive theoretically. The minor presence of  $\text{CH}_3\text{CHDOD}$  in our experiments, the only product that unambiguously can come from reaction R7 (as a deuterated proxy of reaction R2) also encourages us to consider the branching ratio of reactions other than reaction R1 very low, and in the absence of further evidence, negligible. The second interpretation of our results concerns the branching ratios ( $\alpha$  values) of reactions R9-R11. Rationalizing this choice is

<sup>5</sup> In addition to our considerations, the numerical values for the rate constants are gathered in <https://zenodo.org/records/14278652>

easy. If we consider that reaction R8 is the only reaction from the  $\text{CH}_3\text{CHO} + \text{H}$  then, the 90% of remaining  $\text{CH}_3\text{CHO}$  in our hydrogenation experiment (Section 3.2.1) must come from reaction R8 alone. The remaining 10% should be distributed along the different reaction channels R9-R11. It is extremely difficult to determine  $\alpha$  for these reactions experimentally or theoretically. We consider that the best compromise is to equally weigh the remaining 10% along the three different reaction channels. Therefore we recommend setting  $\alpha=0.90$  for R8 and 0.03 for R9-R11.

We would like to indicate that a certain degree of chemical intuition and data interpretation is needed to provide these modeling recommendations. Because our calculations show a significant resistance of  $\text{CH}_3\text{CHO}$  to hydrogenation and deuteration, we interpret our data based on this observation and the evidence from the quantum chemical calculations. Should minor channels along the hydrogenation sequence, for example,  $\text{H}_2\text{CCO}$  hydrogenation reforming  $\text{CH}_3\text{CHO}$  as reported in the literature (Ferro et al. 2023; Fedoseev et al. 2022) have a larger contribution, several of the  $\alpha$  values mentioned above can vary. Nevertheless, we expect these changes to be small.